

## ABSTRACT

LIGUORI-BILLS, NOAH B. Ice Core Records Indicate CMIP6 Emissions Inventories Underestimate Pre-Industrial Biomass Burning. (Under the direction of Dr. Douglas S. Hamilton and Dr. Viney Aneja).

An improved understanding of fire regimes changes from the pre-industrial to the present-day is required to reduce the uncertainty in aerosol radiative forcing over the historical period. Achieving this requires a reassessment of fire emissions in the pre-industrial Era, for which direct observations are scarce at best. Therefore, to assess the current state of assumptions about pre-industrial fire emissions we compared 37 ice core records of black carbon (BC), from sites across every continent except Oceania, to climate model data from three recent climate model ensembles: The Coupled Model Intercomparison Project Phase 6 (CMIP6), the Large Ensemble Community Project (LENS1), and a Community Earth System Model 2 (CESM2) subset of CMIP6. Ice core records record a mean and median 1980/1850 BC ratio of 1.27 and 1.15 for polar cores, compared with 2.89 and 2.64 for the CMIP6 model ensemble respectively. Alpine ice cores record a mean and median change of 2.31 and 1.93 compared to 3.59 and 2.50 for CMIP6. Furthermore, CMIP6 model simulations disagree in the sign of BC change over time in nearly every continent and for all individual ESMs evaluated. Analysis of different drivers suggests that BC emissions in the pre-industrial should be increased in future fire emission datasets in order to reconcile these differences.

© Copyright 2025 by Noah Liguori-Bills

All Rights Reserved

Ice Core Records Indicate CMIP6 Emissions Inventories Underestimate Pre-Industrial Biomass  
Burning

by  
Noah B. Liguori-Bills

A thesis submitted to the Graduate Faculty of  
North Carolina State University  
in partial fulfillment of the  
requirements for the degree of  
Master of Science

Marine, Earth, and Atmospheric Science

Raleigh, North Carolina  
2025

APPROVED BY:

---

Douglas S. Hamilton  
Committee Chair

---

Viney Aneja  
Committee Co-Chair

---

Srijan Sengupta

## **DEDICATION**

To complete this thesis, I intimately studied some of the near-term consequences of the continued combustion of fossil fuels, primarily the melting of alpine glaciers and an increased frequency of extreme wildfires. For this reason, this work is dedicated to everyone building a better world.

## **BIOGRAPHY**

I was lucky to have parents who raised me with a deep appreciation of nature, a value which has been the primary motivator of my academic career. I graduated from the University of Connecticut in 2023 with a Bachelor of Science of Chemistry with minors in computer science and mathematics. A few months later I moved to Raleigh, North Carolina where I completed this thesis under the advisement of Douglas S. Hamilton at NC State University. I plan to expand this work into 3 additional chapters of a PhD.

## ACKNOWLEDGMENTS

I would like to give my foremost thanks to Douglas Hamilton, whose caring support was essential to every step of the process that resulted in this thesis. I would also like to give individual thanks to my committee members including Srijan Sengupta for his suggestions for statistical interpretation and methods, as well as Adrianna Foster and Viney Aneja.

Additionally, I acknowledge the financial and institutional support of NC State University including the Provost's Fellowship awarded to Noah Liguori-Bills, the Marine, Earth, and Atmospheric Sciences Department, and the High-Performance Computing Network.

The CESM project is supported primarily by the U.S. National Science Foundation (NSF). Computing and data storage resources, including the Derecho supercomputer, were provided by the Computational and Information Systems Laboratory (CISL) at NSF NCAR. I thank all the scientists, software engineers, and administrators who contributed to the development of CESM.

All software analysis and figure composition were performed in either Bash or Python, and mainly used the following software packages: netCDF Operators (NCO) (Zender, 2008), Climate Data Operators (CDO) (Schulzweida, 2023), Matplotlib (Hunter, 2007), Cartopy (Elson et al., 2024), InterpolateScalingPy (Liefeld, 2025), Numpy (Harris et al., 2020), and Scipy (Virtanen et al., 2020).

**TABLE OF CONTENTS**

LIST OF TABLES .....	vi
LIST OF FIGURES .....	vii
<b>1. Introduction</b> .....	1
<b>2. Data and Methods</b> .....	6
<b>3. Results and Discussion</b> .....	15
<b>4. Sources of Uncertainty</b> .....	31
<b>5. Conclusion</b> .....	37
<b>6. Future Work</b> .....	38

## LIST OF TABLES

Table A1	Overview of the existing BC ice core model evaluation literature and this work's contribution to the literature.....	75
Table A2	Comparison between different PI and PD averaging methods.....	78
Table A3	Data sources, exact lat, lon positions, and abbreviations of each ice core. ....	78
Table A4	Region definitions and number of ice cores .....	83
Table A5	The ensemble, subset, and comparisons of each model used in this analysis .....	84
Table A6	The max, min, and mean absolute and standard deviation differences between different grid box averaging methods for LENS data. S4 and S8 represent averaging the 4 and 8 nearest grid boxes to an ice core's lat lon respectively, and S1 represents using the raw data from the nearest grid box without any grid box averaging .....	85
Table A7	The absolute and standard deviation differences between different vertical level averaging methods for LENS data. LV30 and LV28 represent nearest and third nearest levels to the Earth's surface respectively .....	85
Table A8	Regional PD/PI BC medians from model variables.....	86
Table A9	Regional PD/PI BC means .....	86

## LIST OF FIGURES

Figure 1	Location of all 37 ice core records of biomass burning .....	8
Figure 2	Definitions of each hemispheric, continental, and emission region used in this study .....	11
Figure 3	Black carbon 1980/1850 ratios of from model anthropogenic emissions (Hoesly et al., 2018), biomass burning (van Marle et al., 2017), and the combinations of the two datasets are shown in the top left, bottom left, bottom right, and top right respectively .....	16
Figure 4	Overestimation and underestimation of CMIP6 anthropogenic and biomass burning datasets relative to ice core ratios .....	18
Figure 5	Modeled and observed 1980/1850 BC ratios across different regions.....	22
Figure 6	Regional differences between model variables and ice core PD/PI BC ratios.....	26
Figure 7	Disagreement between each of the 17 LENS1 transport scenarios investigated (runs 18 through 35) and ice cores .....	28
Figure 8	Differences in the distributions of ice core PD/PI ratios based on the definitions of the pre-industrial (PI) .....	30
Figure A1	Kilimanjaro levoglucosan ice core (Core 9) log scale timeseries smoothed with different lowess smoothing parameters.....	64
Figure A2	Histograms of each ice core's PD value using two different definitions: most recent value (left) and nearest sample date to 1980 CE (right) .....	64
Figure A3	Example of methodology applied to each ice core.....	65
Figure A4	Comparison of averaging techniques for the ice cores' PD and PI.....	66
Figure A5	Histogram of every possible regional division of the Antarctic ice cores.....	67
Figure A6	Histogram of global Hoesly anthropogenic BC emission sources in the PI and PD, highlighting low values less than $10^{-25}$ in the PI that skew PD/PI ratios high ..	68
Figure A7	Using the emissions regions defined in section 2.3, results from Figure 3 were plotted against ice core values in Figure 4 .....	69
Figure A8	Correlation between Greenland ice cores' BC PD/PI ratio and latitude .....	70

Figure A9 Comparison between various LENS variable biases (where $\text{var1} \div \text{var2}$ is labeled as $\text{var1\_D\_var2}$ ) and the ice core .....	71
Figure A10 Relative PD/PI variable ratios. Each plot shows the PD/PI ratio of the variable in the column label multiplied by the ratio of the row label's variable.....	72
Figure A11 Relative PD/PI variable ratios .....	73
Figure A12 BC timeseries used in this work and their 10 and 33 year decompositions .....	74

## 1. INTRODUCTION

Earth System Models (ESM) are powerful tools that can be used to reconstruct and predict the history and future of Earth's climate through the simulation of key processes, including the influence of wildfires and other open burning practices on climate, radiative forcing, and atmospheric composition. To do so, ESMs either use interactive fire models within a land-vegetation model framework or use prescribed gas and aerosol emission datasets that have reconstructed how fire regimes change over a given time period of interest. Of importance for climate studies is understanding how biomass burning (defined here as the sum of all natural and anthropogenic open burning) shapes both the pre-industrial (PI) atmospheric state and how changes in biomass burning alter the atmospheric burden of aerosol and gases over the Industrial Era to the present day (PD) (Carslaw et al., 2013; Hamilton et al., 2018). The Sixth Coupled Model Inter-Comparison Project (CMIP6) experiment is an ensemble of ESMs that produced historical simulated climate relevant data starting in the year 1850 CE. CMIP6 defined 1850 CE as the "Pre-Industrial" for this report based on an assessment of 1850 CE being the beginning of large-scale industrialization (Eyring et al., 2016).

Radiative forcing is a quantification of the change in the atmospheric energy balance between the energy entering and exiting Earth's atmosphere, given in units of  $\text{W m}^{-2}$ . A wide variety of processes can change the energy balance over time, such as human driven alterations to the makeup of greenhouse gases or aerosol in the atmosphere. When the impact of human activity on the energy balance is being quantified it is termed anthropogenic radiative forcing. Understanding changes in biomass burning over the historical period is important for calculating the aerosol radiative forcing as it helps in establishing both a PI atmospheric composition

baseline and the PI to PD aerosol effective radiative forcing (Mahowald et al., 2024; Simpkins, 2018; Wan et al., 2021).

Wildfires directly contribute 2 gigatons of global carbon emissions / year in the PD (van der Werf et al., 2017). Part of the carbon emitted is black carbon (BC) aerosol and in a process known as the aerosol direct effect, this BC aerosol absorbs solar radiation and reemits the energy as heat (Collins et al., 2017). BC can also function as cloud condensation nuclei (CCN) and affect the atmospheric energy balance by changing the cloud drop concentrations and by initiating a series of cloud adjustments that affect cloud albedo (Ackerman et al., 2000; Andreae & Rosenfeld, 2008; Cozic et al., 2007, 2008; Koch & Del Genio, 2010). Furthermore, these aerosols can also change Earth's energy balance when deposited on snow and ice by decreasing surface albedo, and thus, increasing glacial melt rates by absorbing more solar radiation compared to pure ice or snow (Gabbi et al., 2015; Hadley & Kirchstetter, 2012; Hansen & Nazarenko, 2004; Jacobson, 2004; Lee et al., 2013). Through these processes, global BC aerosol have been estimated to contribute  $-0.45 \text{ W m}^{-2}$  effective net radiative forcing from the PI to PD (IPCC, 2021).

One question of particularly high scientific interest is understanding how BC aerosol load, a product of incomplete combustion from both natural and anthropogenic sources, alongside other unique fire combustion products like levoglucosan, has changed over time. In the absence of anthropogenic industrial activity wildfires were a major source of BC aerosol. Wildfire are, together with anthropogenic emission, the major sources of BC aerosol modeled by CMIP6 ESMs, and influenced by both climate conditions and non-climate anthropogenic factors, (Foley et al., 2005; Jones et al., 2022; Mollicone et al., 2006; Pausas & Keeley, 2014; Rudel et al., 2009). The specific effect of each driver depends on the region (Aragão et al., 2018;

Archibald et al., 2010; Baker & Spracklen, 2019; Cahoon et al., 1992; Giglio et al., 2018; Jones et al., 2022; Nikonovas et al., 2020; Staal et al., 2018). The change in wildfires with human population is non-monotonic because increasing human ignitions dominate when population density is low while increasing fire suppression dominates when densities are high (Andela et al., 2017; Archibald et al., 2012; Kelley et al., 2019; Marlon et al., 2008; Pechony & Shindell, 2010). Since the PI, human influences have replaced precipitation as the dominant driver of wildfire regimes (Pechony & Shindell, 2010), causing a global decline in burned area over the 20<sup>th</sup> Century, that has been observed to continue in this century by satellites (Andela et al., 2017). However, the complexity of human drivers of wildfire regime changes over time are often not fully captured in ESMs or in fire BC emission datasets. Not simulating the human driven decline in burned area results in overestimates of the radiative effect of BC aerosol (Hamilton et al., 2018). An improved estimate of the history of BC, and other aerosol or gas emissions, therefore is needed to aid in reducing the uncertainty in the PI to PD effective radiative forcing (Bellouin et al., 2020; Bender, 2020; Rowlinson et al., 2020).

Hamilton et al. (2018) was the first study to evaluate CMIP emission datasets with ice core datasets in an attempt to quantify wildfire emissions' contribution to the uncertainty in PI to PD aerosol radiative forcing (Hamilton et al., 2018). The authors investigated 4 Northern Hemisphere ice-core records using a global aerosol model and discovered that ice cores indicate biomass burning emissions were likely 2x to 4x higher in the PI than the PD than currently estimated in CMIP6. Revised modeling that included fire emission reconstructions that better represented ice core data resulted in reductions of the PI to PD cloud albedo forcing between 35% and 91% compared to using CMIP6 emission data. A follow on study by Liu et al. (2021) focused on the Southern Hemisphere ice core record (Liu et al., 2021). The Authors of that study

investigated 14 Antarctic ice cores and 1 central Andean core from Illimani. Their results supported Hamilton et al. (2018)'s findings that PI biomass burning emissions were likely to be higher in the PI compared to the PD. Their modeling indicated that the decline in the Southern Hemisphere biomass burning BC emissions from 1750 to 2000 was enough to compensate for the change in anthropogenic aerosol radiative forcing over the same period. Other follow on studies include Moseid et al. (2022) who found that cores in the European Alps and Greenland have maximum BC peaks before 1950, agreeing with the charcoal record, while most CMIP6 models give a post 1950 peak (Moseid et al., 2022; Zhang et al., 2024). Other studies have found similar results with different proxy records of burning. For example, Faïn et al. (2025) discovered that the growth rate of Northern Hemisphere carbon monoxide (CO) records (a proxy of biomass burning) and 7 Aerosol Chemistry Model Intercomparison Project (AerChemMIP) models diverge from 1920 to 1980 (Faïn et al., 2025). Charcoal record studies have long supported these conclusions by being some of the first to suggest that global burned area has decreased from the PI to the PD (Arora & Melton, 2018; Marlon et al., 2008). The discrepancies between PI to PD BC changes in CMIP6 and observational ice core records are of timely importance, given plans for the CMIP7 biomass burning BC emissions dataset are still being discussed (Durack et al., 2025).

The growing body of evidence that PI fire emissions were larger than PD has prompted an effort to reconstruct a fire emission inventory that more closely follows proxy record trends. Of note, Zhang et al. (2024) recently used 31 ice core records to reconstruct an improved fire emissions dataset using an inverse modeling framework (Zhang et al., 2024). Zhang et al.'s ice core record shows relatively stable Southern Hemisphere BC from 1750 to 2000 and Northern Hemisphere trends dominated by a large peak in burning around 1920, neither of which are

adequately represented in modeled emissions inventories at present. Another recent study by Guo et al. (2025) reconstructed global monthly burned area from 1901 to 2020 using machine learning models trained with 2003 to 2020 burned area satellite data (Guo et al., 2025). Guo et al. (2025)'s method agreed with many of the findings in Zhang et al. (2024), including a global decrease in burned area from 1901-1978 (Zhang et al., 2024). Most recently, the BuRNN fire model used machine learning models trained on GFED5 data to generate a reconstruction of global burned area from 1901 to 2019, and also supports peak burning occurring in the mid-1900s for several regions including North America and Europe (Lampe et al., 2025). Using an inverse modeling approach with ice cores, CMIP5, and CMIP6 data Eckhardt et al. (2023) created regional BC emissions histories for North America, Europe, Asia, and Russia (Eckhardt et al., 2023). Their North American timeseries showed an increase in burning from 1850 to 1900 followed by declining values until the end of the study period (1995). Eckhardt et al. (2023)'s study individually investigates trends in Russia, where they discover good agreement between ice cores and model values except during the period from 1900 to 1950, which the authors attribute to reductions in anthropogenic burning due to the October Revolution and World War 1. Overall, there is a growing understanding in the literature of discrepancies between observational records of PI fire emissions and model outputs, but more work needs to be done to comprehensively identify its sources.

No study known to the authors has yet investigated all three potential sources of uncertainty in the disagreement between modeled combustion emissions and ice core records: 1. BC emissions datasets, 2. depositional processes, and 3. aerosol transport (Table A1). To explore each of these, this study builds on previous work by assembling the largest fire proxy ice core dataset to date (37 ice cores) and comparing it to 3 ESM ensembles: the Large Ensemble

Community Project (LENS1), CMIP6, and a CESM2 subset of CMIP6. For 1. BC emissions datasets, PI to PD (i.e., PD/PI) BC ratios were calculated for each ice core and compared to the anthropogenic and biomass burning emissions datasets within the local vicinity of Alpine ice cores. The same process was also used for CMIP6 output data and individual variables within its CESM2 subset (BC in the air column, BC in the surface air, BC deposition to snow, and BC in snow) to discern the representation of different BC aerosol processes, addressing 2. depositional processes. As for 3. aerosol transport, individual CESM1 model runs in the LENS1 ensemble, each representing different aerosol transport regimes, were compared to ice core records to assess any role transport may play in explaining model – ice core discrepancies. To qualify these results the uncertainty in the ratios that comes from the definition of the PD and PI are also discussed (Table A2).

## **2. DATA AND METHODS**

### **2.1 Ice Core Data**

Ice cores are usually dated with multiple methods to minimize error, making ice core records of BC emissions a useful tool in the validation of EMSs' modeled history (McConnell, 2010). The most common ice core dating methods used in this study's dataset is radiometric  $\delta^{18}\text{O}$  dating, whose uncertainty depends on the age of ice being dated (Extier et al., 2018). Typical

uncertainties for the study age range (about 200 years ago) range from  $\pm 0.5$  to  $\pm 2$  years per dated layer (Andersen et al., 2006; Eichler et al., 2000).

Data from a total of 36 ice core BC records and 1 levoglucosan record were assembled from the literature for this study (Figure 1 and Table A3). Ice cores were selected for analysis if they met the following criteria:

1. Provided a record of biomass burning (normally BC) within the Industrial Era (defined here as post 1850 CE to follow CMIP6 protocols).
2. The difference between the most recent and oldest years was at least 100 years.

This resulted in at least one ice core being identified within every continent except Oceania (Figure 1). Core 9 in Africa used levoglucosan data as an indicator of burning, instead of BC, because it is the only ice core record of biomass burning in Africa available to the authors at this time. Due to the high variability in levoglucosan records, a LOESS smoothing with a parameter of 0.25 was used to smooth the data prior to analysis (Figure A1).

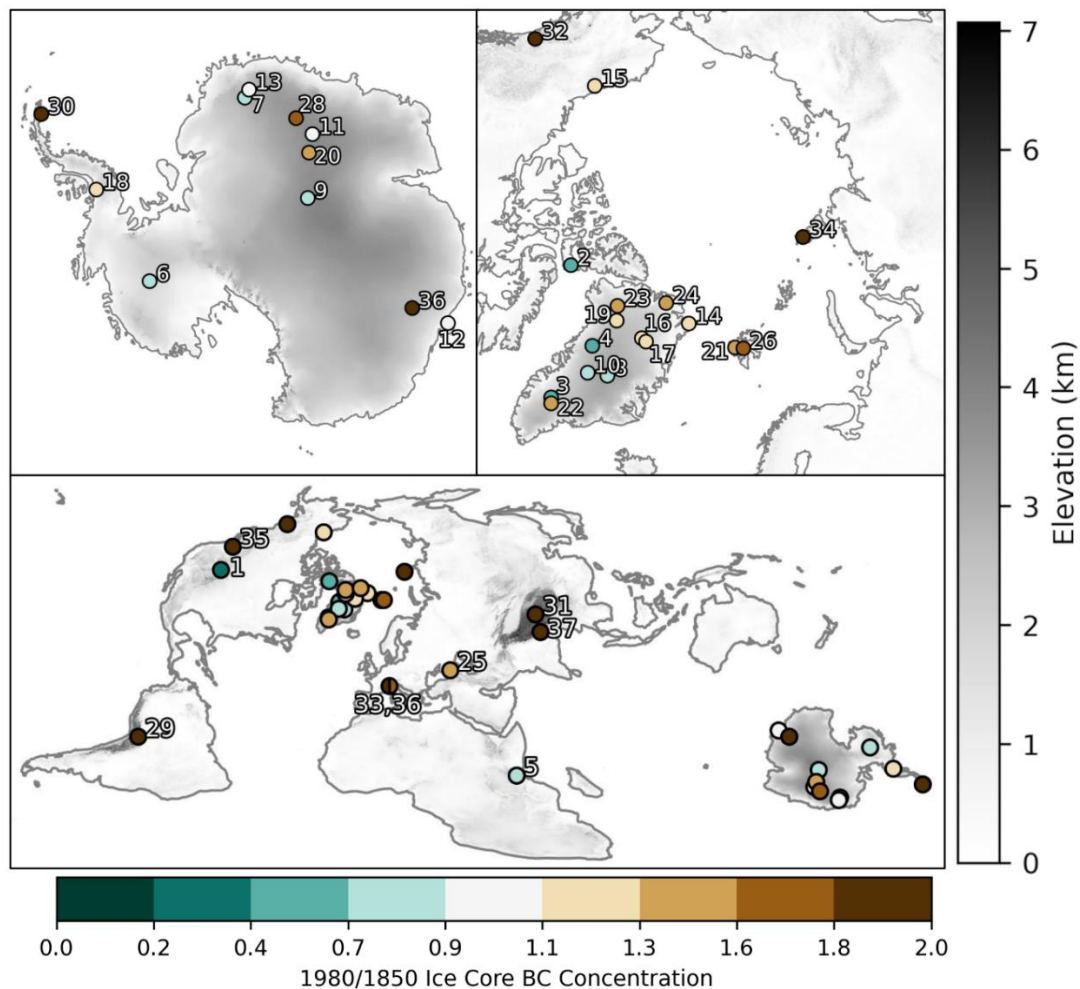


**Figure 1.** Location of all 37 ice core records of biomass burning. Ice core colors represent present day (PD; 1980 CE) / pre-industrial (PI; 1850 CE) black carbon (BC) ratios where blue and brown represent lower and higher BC concentration in the PD relative to the PI, respectively. White represents ice cores with little to no change in BC. Ice core numbers are ordered according to their PD/PI BC ratio where 1 has the lowest ratio (0.40) and 37 has the highest ratio (6.78). Elevation is shown in greyscale. Extended information on the ice cores including their exact location, dating methods, and common naming abbreviations can be found in Table A3.

## 2.2 Defining the Pre-Industrial (PI) and Present Day (PD)

The CMIP6 historical experiment starts in 1850 CE (Eyring et al., 2016). We therefore defined the PI as the 25 years after 1850 CE (inclusive) in order to match the earliest model data

available. The most recent values in the ice core dataset ranged from 1950 to post 2010. The PD was therefore defined as the 25 years preceding 1980 CE (inclusive) because it represented the most recent date where nearly all (36/37) ice cores contained sample data within 5 years of 1980 (Figures A2, A3). 1980 CE also represents a scientific transition point to a new satellite data Era, making assessments of post-1980 changes in atmospheric composition more robust with the advent of a global remote sensing view. Averaging windows from 5 to 30 years were considered for the PI and PD. A 25-year averaging window was ultimately chosen for analysis because it provided the lowest standard deviation across ice core data (Figure A4).

### 2.3 Defining Local, Continental, and Hemispheric Study Regions

This study defines hemispheric regions for broader spatial analysis, including the “North Pole”, “South Pole”, and “Alpine” regions corresponding to ice cores above 66.6° North latitude, within Antarctica, and all other regions combined, respectively (Table A4). Continental regions were defined along standard continent definitions with the exceptions of the Arctic and Greenland. The Arctic continental region was defined as coordinates that were both higher latitude than the Arctic circle (66.6° latitude) and outside of Greenland; five ice cores are located within the Arctic region. Greenland was further separated because Northern and Southern Greenland exhibit differences in seasonal aerosol deposition types and aerosol sensitivities. North Greenland is influenced by high rates of dry deposition during winter months while South Greenland is influenced by high rates of summer wet deposition (Li & Flanner, 2018). Due to these differences in seasonal deposition mode, as well as mean glacier size and cloud cover fraction, Northern and Southern Greenland have been shown to experience different changes in snowmelt and surface energy flux given the same change in aerosol load (Ward et al., 2018). For these reasons, and an abundance of BC ice cores in Greenland (n = 11), the island was divided

into two continental regions: North and South. The Greenland divide falls along  $71.5^\circ$  latitude, the median between Greenland's lowest latitude ( $60.0^\circ$ ) and highest latitude ( $83.0^\circ$ ). Similar to Greenland, previous work has suggested that the East and West Antarctic ice sheets can be considered separately because BC deposition between ice sheets can be uncorrelated and each sheet has been observed to have different BC sources (Bisiaux et al., 2012; Stohl & Sodemann, 2010). However, after testing every possible binary regional division of Antarctic ice cores, the maximum mean PD/PI BC ratio difference was 0.1 (Figure A5). Antarctica was therefore kept as a single continuous region for our analysis. To further understand how emissions sources have changed, continental ice core PD/PI BC ratios were to local upwind PD/PI BC emission ratios.

Squares with 30° longitude and latitude side lengths, centered on the mean coordinate of continental ice core clusters, were used for this local emission change analysis (Figure 2).

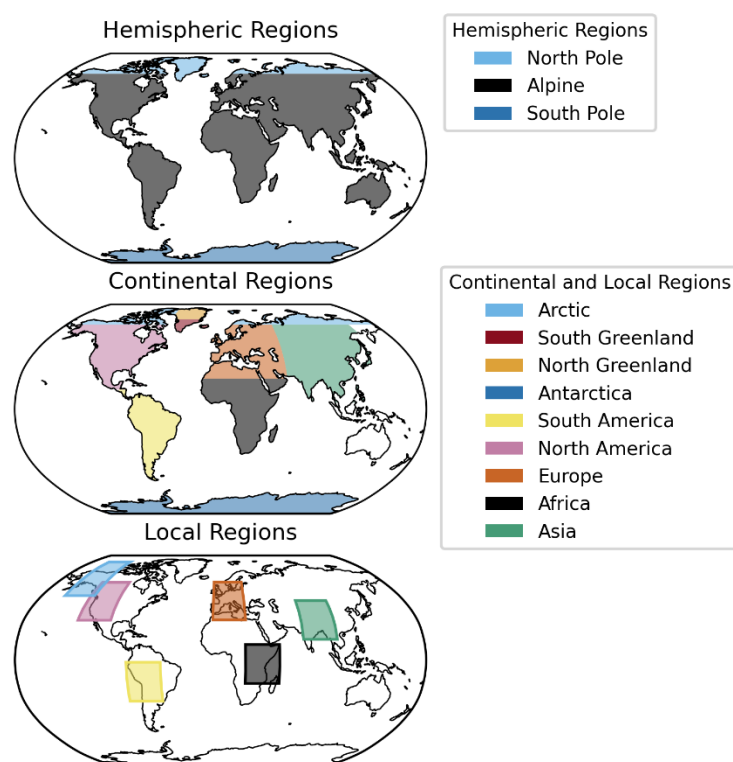


**Figure 2.** Definitions of each hemispheric, continental, and emission region used in this study.

Hemispheric and continental regions are color coded and defined in the legend.

### 2.3 Climate Model Data

Three ESM ensembles were assembled for analysis: the sixth version of the Climate Model Intercomparison Project (CMIP6), a subset of CMIP6 based exclusively on data from the Community Earth System Model version 2 (CESM2), and the Large Ensemble Community Project (LENS). In order to quantify projected future changes and past reconstructions of the state of the Earth System and its climate, CMIP employs an ensemble of ESM's (Eyring et al.,

2016; Lamarque et al., 2013). Data from the CMIP6 historical experiment was used herein because it provides model data from 1850 to 2014 and represents the most recent assessment. The comparison of CMIP6 ESM results to ice core BC required identifying those models that provided BC deposition data; seven were identified consisting of CESM2 (Kay et al., 2015), CanESM5 (Swart et al., 2019), MIROC (Kawamiya et al., 2020), EC-Earth3 (Döscher et al., 2022), MRI (Yukimoto et al., 2019), CNRM (Roehrig et al., 2020), and IPSL (Boucher et al., 2020). In addition to contributing to CMIP6, the CESM2 (and sister ESM models based on it) were separately analyzed because they additionally provided data on snow and atmospheric burden BC variables (termed soot<sub>sn</sub> and load<sub>bc</sub>, respectively). LENS is an ensemble of CESM2 simulations initialized with  $10^{-14}$  K differences in air temperatures (Kay et al., 2015). There is no difference in the CESM2 model versions in any of the LENS ensemble members, so in terms of BC analysis differences between each run only represent changes in transport induced from a perturbed initial condition. Despite only small initial condition changes, some LENS ensemble members have been reported to produce unrealistic temperature profiles (REF); therefore, comparison of LENS data to ice cores is undertaken with the full LENS ensemble dataset.

The CMIP6 wet and dry BC deposition variables were the most common variables among models, and so deposition forms the main CMIP6 comparison variable. The only BC indicator available in LENS was aged BC concentrations at the surface. As most ice cores are far from emission source, we assume that the omission of hydrophobic (or freshly emitted soot) data is minimal in the analysis of LENS data. In addition to comparing all models to each other, 4 model variables within the CESM2 subset were also compared: BC in air column (load<sub>bc</sub>), BC in surface air (mmr<sub>bc</sub>), BC deposition (dry<sub>bc</sub>-wet<sub>bc</sub>), and BC in snow (soot<sub>sn</sub>). A complete list of

individual models used and the ensembles, subsets, and comparisons they belong to can be found in Table A5.

CMIP6 used two datasets for reconstructing the history of aerosol and gas emissions from PI to PD: a biomass burning emission dataset (van Marle et al., 2017) and an anthropogenic emission dataset (Hoesly et al., 2018). The biomass burning dataset was constructed by combining post-1980 satellite-based estimates of fire emissions from the Global Fire Emissions Database version 4s (GFED4s) with a pre-1980 reconstruction based on the charcoal record, World Meteorological Organization (WMO) visibility observations in South America and Indonesia, and the average of six fire models from the Fire Model Intercomparison Project (FireMIP) (Rabin et al., 2017). The anthropogenic dataset was constructed by combining historic fuel use and manufacturing data calibrated against existing emissions inventories, and was organized by year, country, and sector.

#### 2.4 Comparison of The Pre-Industrial and Present Day

The PD/PI BC ratio was calculated using a 25 year mean in each time period (Equation 1 and Figure A3). The data output from ESMs is organized into grid cells using cartesian coordinates and so the PD/PI BC ratio was calculated using the grid cell co-ordinate that included each ice core's latitude and longitude. Emissions dataset PD/PI ratios were calculated using the emission means calculated across each region as defined in Figure 2. To represent BC in the surface air, only the surface level concentration was used from the vertically distributed data. No meaningful difference was found between these methods and alternative grid box averaging or vertical level methods (Table A6 and A7).

$$\frac{\text{PD}}{\text{PI}} = \frac{\overline{[BC]_{1955-1980}}}{\overline{[BC]_{1850-1875}}} = \frac{\frac{1}{25} \sum_{yr=1955}^{1980} [BC]_{yr}}{\frac{1}{25} \sum_{yr=1850}^{1875} [BC]_{yr}}$$

**Equation 1.** Definition of the PD/PI ratio where 25-year means are taken around the pre-industrial “PI” (1850-1875) and the present day “PD” (1965-1980). “[BC]” represents whatever BC analog is under investigation, BC concentration, levoglucosan concentration, or various model variables for BC ice cores, the African ice core, and models respectively.

To determine if ESM regional means are larger than ice core means globally, a paired T-test was used with “ice core mean > ESM mean” set as the alternative hypothesis. The T-test was implemented with SciPy’s `ttest_rel` function, and was reported as significant if the resulting P value was below 0.05 (Virtanen et al., 2020).

### 2.5 Comparing Biomass Burning vs. Anthropogenic BC Emission Sources

All CMIP6 models are forced with biomass burning emissions from (van Marle et al., 2017) and anthropogenic emissions from (Hoesly et al., 2018). These datasets allow a direct comparison of historical estimates of BC from biomass burning and anthropogenic activity to the total BC observed in ice cores. Data from these emission sources were converted into PD/PI BC ratios (Section 2.4). In many locations anthropogenic PI emissions were lower than  $10^{-25} \text{ kg m}^{-2} \text{ s}^{-1}$ , skewing PD/PI ratios high with such a low dominator (Figure A6). To account for this while preserving the temporal change in anthropogenic emissions, PI biomass burning emissions were added to both the PD and PI anthropogenic values in results labeled “Anthropogenic+BiomassBurning<sub>PI</sub>”. This is compared to the direct some of the two datasets labeled “Anthropogenic+BiomassBurning”.

### 3 RESULTS AND DISCUSSION

#### 3.1 Biomass burning vs anthropogenic emissions of black carbon from 1850 to 1980

Both biomass burning and anthropogenic activity are sources of BC to the atmosphere.

To first examine the individual contributions of each BC source in CMIP6 emission datasets we compare the anthropogenic, biomass burning, and total PD/PI BC emission ratios (Figure 3). As to be expected, anthropogenic BC emissions have globally high PD/PI ratios due to the large increases in anthropogenic activity producing BC emissions occurring post-1850. The mean PD/PI ratio in anthropogenic BC emissions is above 100 in all six regions analyzed (Figure A7). In contrast, the PD/PI ratio in biomass burning emissions is only greater than a factor of 2 within Equatorial Asia, falling between 0.4 and 1.1 in the Northern Hemisphere and between 0.9 and 2.0 in the Southern Hemisphere. To investigate whether anthropogenic PD/PI BC emission ratios were being skewed by very low PI values between 1850 and 1875, PI biomass burning BC emissions were added to the anthropogenic PD and PI BC emission values individually (Figure 3). The combined BC PD/PI ratio in fire affected regions, including high latitude forests, Central and Southwest Africa, Australia, parts of the Amazon, and Southeast Asia, falls closer to 1 as a result. However, in heavily industrialized, populated, or farmed regions the PD/PI ratio remains above a factor of 2.

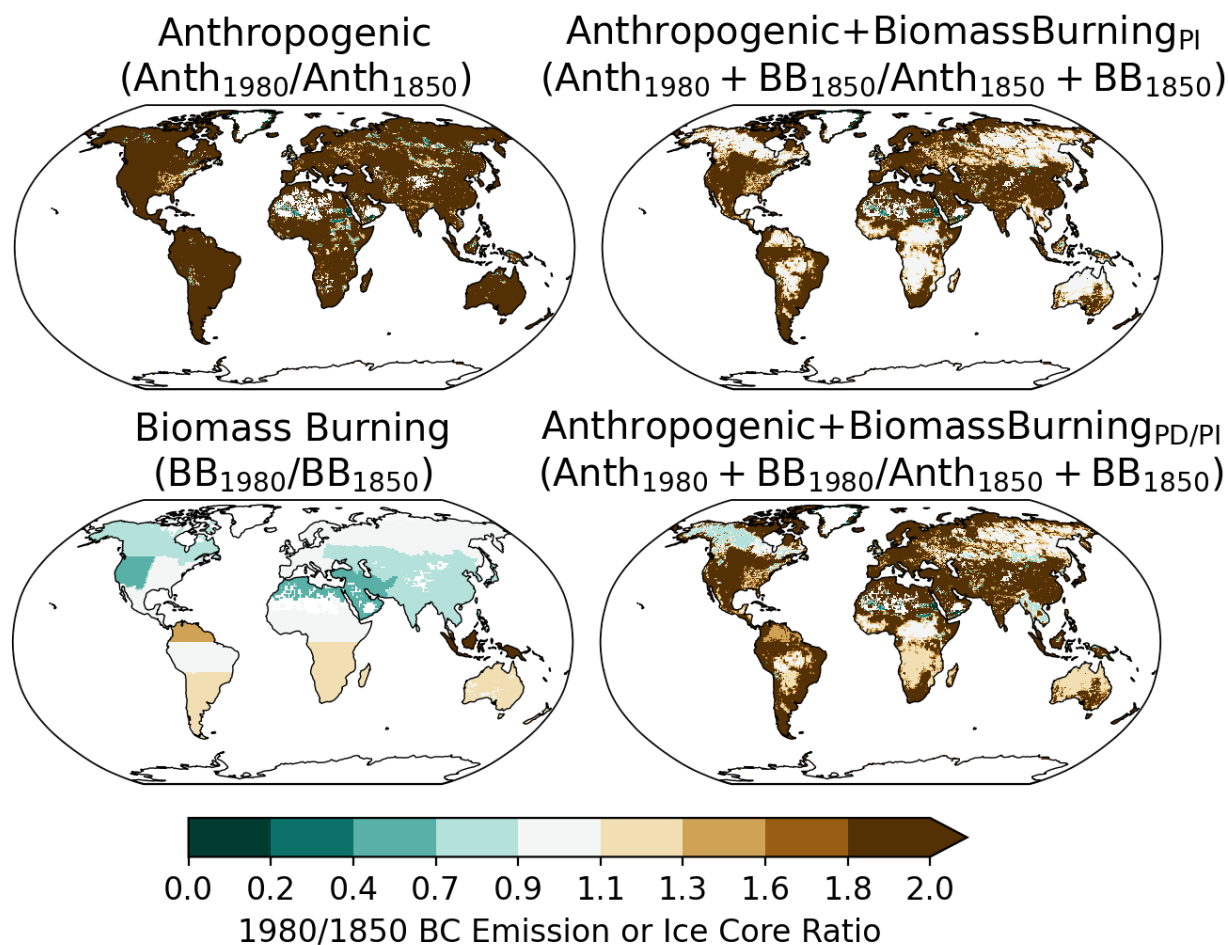


**Figure 3.** Black carbon 1980/1850 ratios of from model anthropogenic emissions (Hoesly et al., 2018), biomass burning (van Marle et al., 2017), and the combinations of the two datasets are shown in the top left, bottom left, bottom right, and top right respectively. The equations used to calculate each dataset's ratio is listed in parenthesis below each title. Biomass ratios are all below 1.6 while most anthropogenic values are above 2.

To understand how BC emission datasets compare to BC recorded within ice cores, ice core PD/PI ratios were compared to the corresponding range in BC ratios from ice cores (Figure 4). The anthropogenic emissions dataset, as well as the Anthropogenic+Biomass<sub>PD/PI</sub> both show a mean ratio above 100 (Figure A7). Anthropogenic BC PI values are expected to be low uncertainty because anthropogenic BC emissions in the PI are near zero and are well documented

and easier to measure in the PD. One exception to this assumption is biofuel, which was a non-zero BC emission source in the PI, but since global populations were low in 1850, biofuel's contribution is assumed to be negligible compared to the PD (Goldewijk, 2005). Similarly, ice core BC (with a maximum PD/PI ratio of 6.78) and PD biomass burning are also assumed to be well constrained, leaving PI biomass burning as the major source of BC uncertainty. The well constrained nature of PD/PI anthropogenic BC ratios and biomass burning PD values suggests that PI biomass burning emissions are currently underestimated, leading the mean biomass PD/PI ratio of 0.90 to be insufficient in bringing total BC emissions near ice core ratio values.

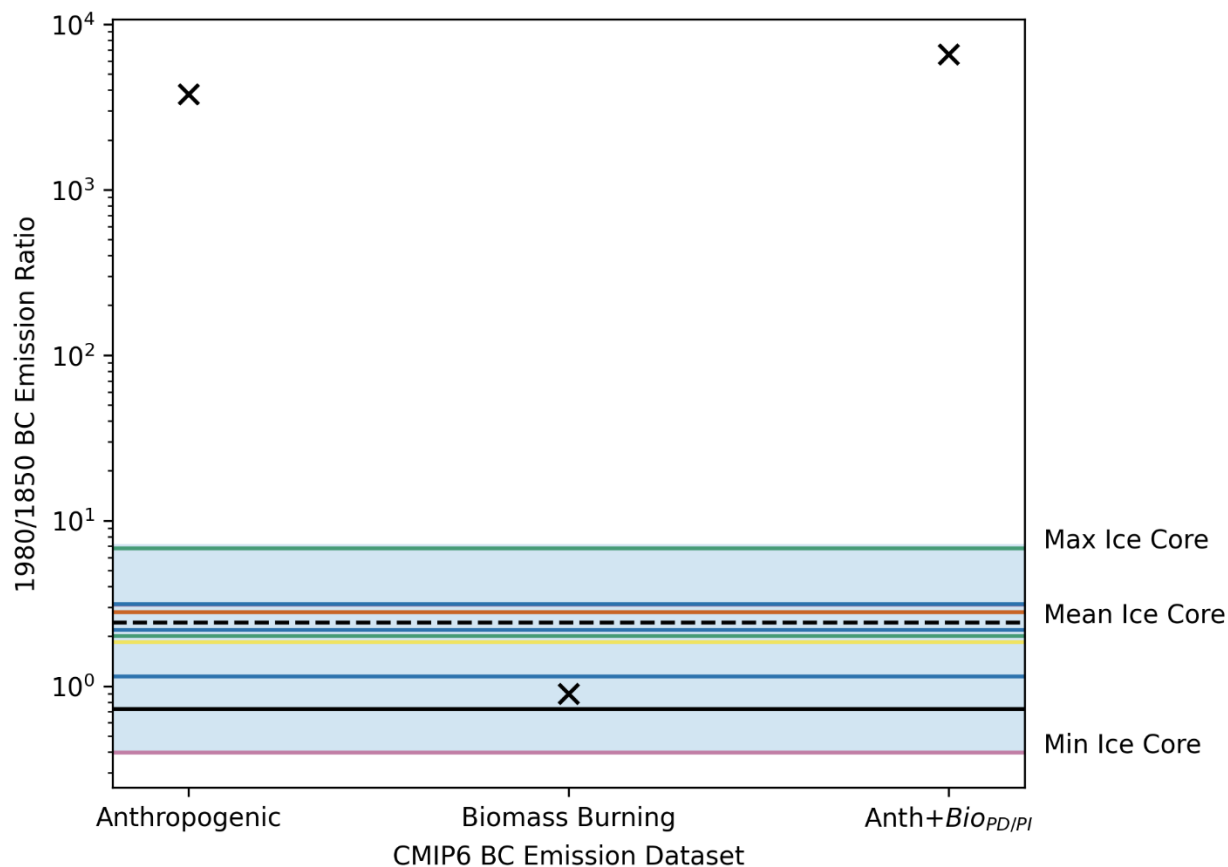


**Figure 4.** Overestimation and underestimation of CMIP6 anthropogenic and biomass burning datasets relative to ice core ratios. Each X represents the mean BC emission ratio from the bounding boxes around the corresponding ice cores (Figure 2). Horizontal lines represent ice core ratios.

### 3.2 CMIP Models Overestimate PD/PI BC Ratios in Nearly Every Region of the World

A comparison of ice core BC ratios to emission datasets alone does not account for modeled transport and depositional processes that can alter the ratios in downstream ESM variables. For these reasons, CMIP6 modeled PD/PI BC deposition ratios were compared to those obtained from the ice cores, producing results indicating that CMIP6 models overestimate the BC ratio in nearly every region of the world (Figure 5). Globally, the mean PD/PI BC ratio in

the ice cores is 1.55 while the model ratios are at least twice as high, CMIP6=3.08 and LENS =5.80. The CMIP6, and LENS multi-model mean ratios are twice or higher at 3.08, and 5.80, respectively. Model medians and means in 30/37 ice cores analyzed are above the ice cores' inter quartile range. The modeled ratios at single ice core locations are frequently above 3, and in many regions the lowest modeled value is higher than the highest ice core value.

In North Greenland, ice core ratios have a mean and median of 1.13 and 1.17 respectively and a narrow first to third quartile range of 1.06 to 1.28. No modeled ratio is within North Greenland ice core's first to third quartile range or overall range (0.54 to 1.52). CMIP6 and LENS have North Greenland medians of 2.96, and 7.94 respectively. Similar means and medians (0.93 and 0.88) are seen in South Greenland as well as a narrow first to third quartile range of 0.68 to 1.17 around a mean and median of 0.93 and 0.88. LENS' mean and median are 4.93 and 5.48 respectively, but only a single modeled ratio in LENS is within the ice cores first to third quartile range. Notably ice cores and every model show slightly lower ratios in South Greenland compared to North Greenland, supporting latitude based differences in the region's seasonal aerosol deposition types and aerosol sensitivities (Li & Flanner, 2018; Ward et al., 2018). Greenland's latitude based differences in ice core PD/PI ratios can be seen in Figure A8 where ice core PD/PI ratios show a correlation with latitude of  $R^2 = 0.24$ , agreeing with previous work that has found a latitude based difference in Greenland's BC aerosol deposition seasonality and sensitivity (Li & Flanner, 2018; Ward et al., 2018). In the Arctic, which consists of the 5 remaining ice core locations that are both above the Arctic circle and outside of Greenland, ice core PD/PI ratios have a median value of 1.41 (and a similar mean of 1.49), a range from 0.43 to 2.82, and a first to third quartile range from 1.14 to 1.67. CMIP6 mean and median (2.23 and 2.00 respectively) are above the ice core's (1.49 and 1.41 respectively) in the Arctic, and only

2/5 CMIP6 ratios fall within the ice core's first to third quartile range. LENS displays a larger range in the Arctic than in any other region with a min and max ratio of 0.77 and 19.02, respectively, representing a factor of 25 uncertainty. LENS displays a large range of PD/PI ratios throughout this study's data analysis, so the large range observed in the Arctic most likely represents the range of transport deviations created by its initial temperature differences (Section 3.4) rather than any unique property of the Arctic (Figure A9). North and South Greenland show the most robust difference between all model and ice core ratios. Although Antarctica represents BC ratios from different source regions, the differences between ice core and model ratios are similar to those found in the Arctic regions. Antarctic ice cores have ratio means and medians of 1.36 and 1.05, respectively, and a first to third quartile range from 0.92 to 1.56, respectively. CMIP6 has one ratio within the ice core range, and a mean and median of 2.70 and 2.64, respectively. LENS shows 2 ratios within the Antarctic ice core range and 3.78 and 2.54 for its mean and median, respectively. The general similarity in the ice core-model differences of Antarctica and the Arctic regions suggests that there is a global model bias.

Alpine regions have fewer ice core locations per region and show more varied ratios than in the poles. In Africa, where only a single ice core was available, CMIP6 and LENS, ratios are 4.42, and 0.80, respectively, compared to the ice core value of 0.72. Asia is one of two regions that show good agreement between ice cores and models. Asian means for CMIP6 and LENS are 3.29, 6.83, respectively. We do not calculate medians in Asia because only two ice cores are available. The high agreement in Asia is most likely due to the region's large increase in biofuel combustion from the PI to the PD. Europe is the second region with good agreement and means of 1.53, 1.74, and 2.0 for CMIP6, LENS, and ice core record respectively. Ice cores in the region have a median of 1.9 and a first to third quartile range of 1.29 to 2.65 where CMIP6 and LENS

have medians of 6.31, and 8.67, respectively. In South America the single ratio for the ice core record, CMIP6, and LENS are 1.84, 1.39, and 17.93, respectively. Overall, the CMIP6 and LENS in Europe and CMIP6 alone in South America are only regions where modeled medians are lower than ice cores’.

Changes in land use from the PI to PD can help explain the range of Alpine ice core-model ratio differences. By 1850 CE, Europe had already experienced the land use transition that was responsible for many of the high PI BC ice core values in other regions (Kaplan et al., 2017). In contrast, the timing of North America’s colonial land clearing based combustion can help explain why it is the region with the largest difference between models and ice cores (Ryan et al., 2013).

The timing of European and North American land use transitions is in agreement with the finding that CMIP6 model emissions overestimate BC emissions and that human driven changes on wildfire regimes are the source of this discrepancy, from the four previous studies that evaluated climate models using ice cores (Hamilton et al., 2018; Liu et al., 2021; Moseid et al., 2022; Zhang et al., 2024) as well as the larger body of literature that indicates a global decrease in biomass burning from the PI to the PD. The time series in Zhang et al., (2024) showed similarly large rates of biomass burning BC in the PI (Zhang et al., 2024). Our global decrease in burning also supports the 1901 to 1978 decrease found by Guo et al., (2025) as well as the post 1850 North American decline in biomass burning found in the inverse modeling study by (Eckhardt et al., 2023; Guo et al., 2025).

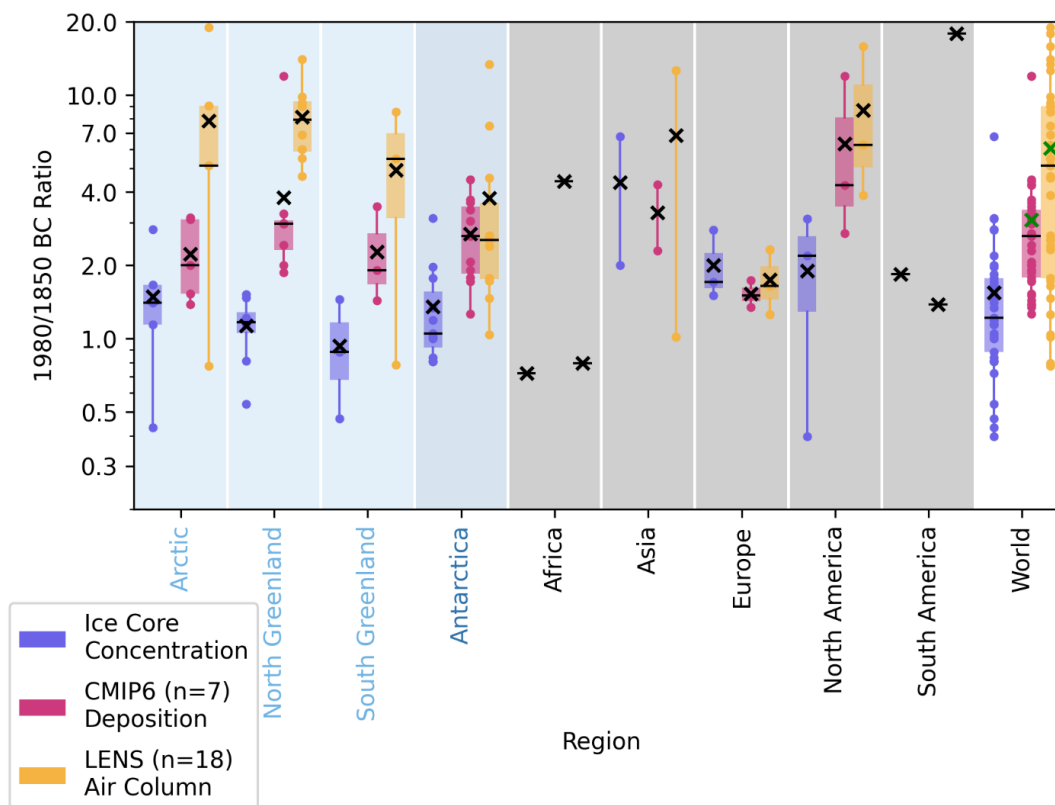


**Figure 5.** Modeled and observed 1980/1850 BC ratios across different regions. Ice core ratio is based on BC concentrations, CMIP6 is based on modeled BC deposition, and LENS is based on BC in the air column. Each data point represents either a measured ice core PD/PI ratio or the modeled PD/PI ratio within the grid cell containing an ice core's location. Medians, means, and data points are represented by black vertical lines, X's, and colored points, respectively. Whiskers extend to the farthest data point within 1.5 times the inter-quartile range. Ice cores, CESM2, CMIP6, and LENS ratios are colored blue, orange, red, and yellow, respectively. Background bar colors denote if the region is in the Arctic, Antarctic, or neither (light blue, dark blue, and grey, respectively). Regions with two data points show only the two points connected by a line and their mean value. Regions with a single data point are represented by a colored X and a black line. Global model means are colored green to highlight statistical significance ( $P < 0.05$ ) between model and ice core means.

### 3.3 Comparison of aerosol concentration and deposition PD/PI ratios

After BC aerosol is emitted to the atmosphere, it undergoes three sequential processes that can result in ice-based preservation: transport, deposition, and glaciation. When suspended in the atmosphere, BC has a residence time of between a few days to a couple of weeks (Cape et al., 2012) during which it can be chemically transformed, including from an initial hydrophobic phase to a hydrophilic one, and transported long distances by several mechanisms such as low altitude transport, transport with ascent at the Arctic front, or ascent at the emission source (Stohl, 2006). Ultimately, all BC aerosol emitted to the atmosphere is deposited back to the Earth's surface through either wet deposition, involving precipitation, or dry deposition, involving gravitational settling, Brownian motion, impaction, or interception (Seinfeld & Pandis, 2016). PI BC baseline uncertainty therefore lies not only in the observational uncertainty of each of these post-emission aerosol processes (Browse et al., 2012), but also in how they have changed over time and ESMs abilities to simulate them and their change.

To investigate how individual modeled aerosol processes relate to the discrepancy between modeled and observed ratios, a series of key aerosol process variables from the CESM2 (a subset of CMIP6) were investigated (Figure 6). Only the CESM2 is used because it was the only CMIP6 model dataset that contained each of the 4 variables under investigation: (1) BC in air column (model variable name: loadbc); (2) BC in surface air (model variable name: mmrbc); (3) BC deposition (model variable names: drybc and wetbc); and (4) BC in snow (model variable name: sootsn). Their order generally corresponds to how closely each variable is expected to physically represent BC in an ice core, where BC in the air column is the furthest and BC in snow is the closest to BC in an ice core (Table A8). It should be noted that the CMIP6 variable “sootsn” (BC in snow) is defined as “soot\_content\_of\_surface\_snow” (van den Hurk et al., 2016)

and so this variable does not directly correspond to measurements of ice core BC because firm densification processes can alter BC concentrations by up to three orders of magnitude between fresh snow and granulated ice (Kang et al., 2020; Schmitt et al., 2019; Xu et al., 2012).

In general, median PD/PI ratios from BC in air column, BC deposition to snow, BC in surface air, and BC in snow are more similar to each other than to the ice core ratio (Figure 6). Regional ice core PD/PI ratio medians range from 1.05 to 1.93 and the corresponding values from model variables are 1.91 to 3.90. A complete list of medians is given in Table A8. Every model variable's median PD/PI ratio in every region is above the ice core's third quartile in the corresponding region. All variable means except BC in snow are significantly ( $P < 0.05$ ) larger than ice core values in polar regions, and BC in air column is significantly larger in Alpine regions. BC in air column and BC in surface air show median ratios with each other's first to third quartile range in the North Pole and South Pole, but not the rest, where BC deposition to snow and BC in surface air share that property. In the North Pole and South Pole, all variables show the same relative relationship where BC deposition to snow, BC in air column, BC in surface air, and BC in snow show decreasing medians in that order. This trend does not hold in the rest, where BC in surface air and BC deposition to snow have medians within each other's first to third quartile range, and otherwise the trend is reversed. Figures A10 and A11 show ratios between modeled variables across the globe.

The literature has investigated uncertainty of "in air" model variables what the houseseparately from "in snow". The most representative variable to ice core BC in CMIP6 models could be argued to be sootsn, but the uncertainty in CMIP6 sootsn has only been evaluated by two studies. Chen et al. (2022) found that spatial-temporal patterns of CMIP6 sootsn agreed well with snow BC concentration observations from 1980 to 2014 (Chen et al.,

2022), with generally increasing trends over the study period, although there was considerable disagreements between models (CESM2, CESM2-FV2, CESM2- WACCM, CESM2- WACCM-FV2, NorESM2-LM, NorESM2-MM, and TaiESM1), especially in Europe and Asia which showed standard deviations of  $200 \text{ ng g}^{-1}$  (relative standard deviation=300%). Chen et al., (2024) found that CMIP5 and CMIP6 models struggled to reproduce inter decadal variability in global snow BC concentrations, especially in Antarctica where CMIP6 overestimated snow BC radiative forcing by 144% (Chen et al., 2024). The authors identified post depositional snow processes as the largest sources of large-scale model errors, rather than the other aspects of land component of models, which show good agreement with observations (Chen et al., 2024; Ma & Wang, 2024).

Although BC in snow is the only variable that is not significantly ( $P < 0.05$ ) greater than ice core ratios, it is not as well evaluated as BC in the air column, and can contain downstream uncertainties from other processes such as meteorology (Zhang et al., 2022). Additionally, BC in snow is only available in model grid cells that have a substantial fraction of their landcover covered in snow, which is why the variable has fewer datapoints in all three regions shown in Figure 6. For these reasons, BC in snow may not actually represent good agreement between ice cores and ESMs. These sources of uncertainty can explain some of the difference between soot<sub>sn</sub> and the other model variables, but large discrepancy between all four model variables and the ice core values present in each of the hemispheric regions is most likely due to an error in the BC emissions dataset rather than a physical process modeled by an ESM.

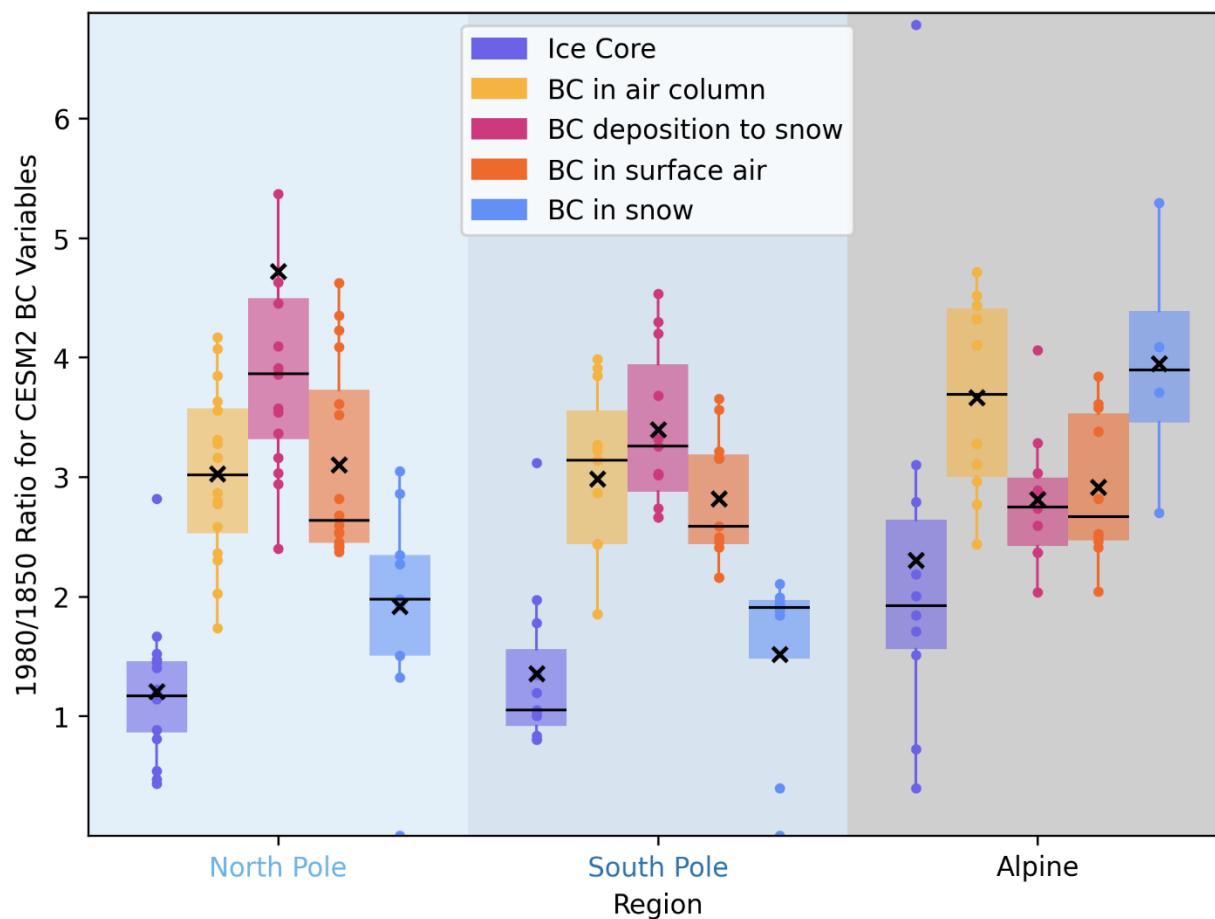


**Figure 6.** Regional differences between model variables and ice core PD/PI BC ratios. Each data point represents either an observed or modeled PD/PI BC ratio at one ice core's location.

Medians, means, and data points are represented by black vertical lines, black X's, and colored points respectively. The box of the boxplots represent the range from the first quartile to the third quartile, and the whiskers extend to the farthest data point within 1.5 times the inter-quartile range. Ice core, BC in air column (loadbc), BC in surface air (mmrbc), BC deposition to snow (drybc-wetbc), and BC in snow are colored dark blue, red, orange, yellow, and light blue respectively. Background bar colors correspond to the region.

### 3.4 Influence of transport on modelled deposition ratios

An alternative explanation for the discrepancy between modeled BC ratios and ice cores is that BC aerosol transport, from emission to deposition, over the historical period is significantly different from what is being simulated by CMIP6 models. To explore the role of transport we used the LENS ensemble. LENS is an ensemble of 35 CESM2 runs, identical in all respects except for a very small variation in the initial atmospheric temperature on the order of  $10^{-14}$  K. These small perturbation to the initial condition results in variations in meteorology (Kay et al., 2015), and therefore in aerosol transport pathways. Individual LENS run comparisons with ice cores are shown in the sixth to last columns of Figure 7. The number of ice core locations where each modeled PD/PI ratio is within 0.25 of the ice core value (pink cells) is shown in the last row. The maximum number of ice core locations where ice core ratios were near LENS values is 9/37 (i.e., ~25%), seen in both runs 19 and 25. However, runs 19 and 25 also contain 7/37 and 6/37 ratios above 9, which is far outside of the ice core range whose maximum is 6.78. All the other 17 runs investigated had 5/37 or less ice core locations where ice core ratios were near LENS values and a total of 158/629 (~25%) ratios above 9. The average LENS run used in other analysis sections has three locations where ice core ratios are within 0.25 of modeled values, and 10/37 ratios above 9. These results indicate that no variation in transport regime improves ESM agreement with ice cores, and therefore transport can't explain the discrepancy between ice cores and modeled values.

Ice Core Index	Ice Core	CMIP6	CESM2	LENS	LENS18	LENS19	LENS20	LENS21	LENS22	LENS23	LENS24	LENS25	LENS26	LENS27	LENS28	LENS29	LENS30	LENS31	LENS32	LENS33	LENS34	LENS35
1.0	0.396	2.988	3.034	9.3	9.982	5.361	7.595	8.559	7.502	8.455	12.27	9.372	11.573	9.323	7.338	5.051	10.952	7.8	12.418	10.14	12.192	11.52
2.0	0.432	3.732	3.909	1.778	0.42	1.436	0.599	3.542	0.975	0.532	1.079	3.788	1.003	1.664	1.82	1.478	0.375	2.962	3.947	1.766	1.008	3.609
3.0	0.47	11.963	10.189	14.023	9.249	19.266	12.375	22.178	11.347	9.621	15.39	10.318	10.091	8.274	17.825	15.811	15.359	22.56	12.513	12.717	9.636	17.879
4.0	0.54	3.493	4.453	5.477	1.099	12.916	3.045	22.316	5.856	2.459	5.433	0.994	1.406	3.906	13.06	2.282	1.976	8.194	3.403	5.066	3.512	1.657
5.0	0.724	4.264	4.059	3.882	4.06	2.296	4.573	3.532	3.455	3.393	3.596	5.142	4.924	3.294	4.242	3.568	5.256	3.374	5.054	3.019	3.657	3.446
6.0	0.805	1.913	2.738	0.78	0.755	0.704	0.457	0.667	0.91	0.734	0.849	0.855	1.005	0.845	1.27	0.544	0.513	0.723	0.76	0.491	1.016	0.936
7.0	0.807	1.387	2.661	17.926	53.66	0.538	13.274	21.706	7.996	1.502	12.432	30.412	21.141	8.747	2.153	39.054	11.215	27.309	5.751	20.573	8.418	36.785
8.0	0.812	3.255	4.628	9.026	2.328	8.155	4.278	46.906	8.502	2.794	6.871	1.374	7.454	5.112	22.542	7.213	3.363	11.36	4.483	7.445	6.431	5.864
9.0	0.838	2.299	3.683	1.018	1.236	1.285	1.037	1.392	1.021	1.479	0.289	0.512	1.288	0.21	0.103	0.551	0.842	0.712	1.693	2.685	1.308	0.683
10.0	0.884	4.285	5.366	12.634	4.984	14.569	8.265	50.855	13.075	9.126	11.243	6.347	12.647	7.797	14.893	10.874	6.955	16.38	7.416	13.147	8.831	9.999
11.0	1.0	1.507	3.018	1.65	2.872	0.88	0.541	1.33	2.301	8.639	0.599	0.164	0.362	0.207	2.276	0.94	1.159	0.899	2.955	1.361	1.08	1.136
12.0	1.022	1.348	4.203	2.32	1.116	2.147	1.777	0.879	2.445	1.948	2.443	2.072	0.48	2.561	2.575	1.184	3.31	6.29	5.686	0.908	2.42	1.528
13.0	1.05	1.387	2.661	19.019	50.331	0.421	16.703	32.477	9.365	4.792	22.152	30.302	32.165	3.004	3.28	38.405	10.855	18.05	8.256	16.001	18.463	27.311
14.0	1.142	2.423	3.035	4.657	0.904	6.174	6.305	5.27	3.633	0.992	10.025	1.56	4.379	4.572	3.195	1.535	7.03	5.261	6.765	1.579	1.365	13.286
15.0	1.145	2.638	2.399	7.479	4.949	9.595	5.71	7.859	14.648	18.812	2.536	1.549	7.239	1.154	9.162	7.047	8.257	8.305	6.786	2.818	9.067	9.13
16.0	1.148	2.96	3.869	6.006	2.619	5.218	5.69	8.307	4.943	12.537	6.485	0.981	2.626	4.26	8.239	1.515	3.829	19.232	4.892	2.722	4.935	9.08
17.0	1.186	2.96	3.855	6.859	3.302	5.37	5.428	4.884	5.249	15.012	6.744	1.254	3.608	2.975	12.472	1.971	4.638	21.801	5.226	3.575	5.811	10.547
18.0	1.194	1.527	3.322	0.775	0.78	1.096	0.591	0.377	0.772	0.784	0.682	1.013	1.102	0.994	1.032	0.512	0.253	1.004	0.582	0.774	0.776	0.824
19.0	1.222	3.094	4.095	5.14	1.04	10.865	2.276	9.351	3.728	7.026	6.501	1.272	2.538	4.657	1.885	1.443	3.069	12.149	6.269	2.467	4.583	11.41
20.0	1.343	1.738	3.253	1.258	3.521	0.995	0.784	0.823	0.828	3.814	0.698	0.331	1.767	0.114	3.005	0.53	1.057	0.805	1.205	1.255	0.643	0.469
21.0	1.407	3.389	3.162	2.541	1.402	4.771	1.108	1.996	1.103	1.8	2.807	0.884	3.357	1.809	1.757	2.398	10.484	1.385	3.532	1.916	1.367	1.864
22.0	1.45	11.963	13.178	15.874	12.345	20.645	12.856	16.912	15.081	14.392	20.182	10.191	17.455	13.463	18.806	16.149	14.847	19.406	14.841	16.221	13.479	18.457
23.0	1.474	3.142	3.541	5.141	1.671	6.852	3.019	11.81	3.714	9.854	4.541	1.498	2.896	4.24	5.686	1.909	2.739	10.931	9.361	2.953	2.658	6.199
24.0	1.509	2.066	2.367	13.369	12.165	11.082	9.581	9.452	8.149	7.439	9.536	9.391	8.379	8.574	39.516	16.434	14.766	29.758	10.428	20.058	6.932	8.999
25.0	1.523	2.706	2.944	6.25	1.61	5.66	16.969	1.346	5.39	16.088	17.67	2.238	3.368	4.031	7.655	1.566	4.373	3.324	6.489	2.449	3.117	9.162
26.0	1.665	3.615	3.367	2.555	1.289	4.937	1.236	1.581	1.028	1.902	4.162	0.841	3.595	1.878	1.467	2.116	11.517	1.073	2.424	1.538	1.389	2.01
27.0	1.71	2.001	2.763	9.072	8.629	11.014	7.598	5.169	6.575	9.866	7.318	4.033	22.144	7.403	11.149	19.924	6.28	6.786	10.325	6.399	3.523	9.155
28.0	1.777	1.267	3.028	4.57	1.022	1.046	2.86	3.627	1.087	2.481	13.209	0.488	5.625	0.681	2.397	3.805	13.252	1.107	10.763	10.413	4.302	4.093
29.0	1.845	4.424	2.738	0.795	0.511	1.024	0.291	1.035	0.559	0.862	0.645	0.742	0.874	1.205	1.491	0.841	0.591	0.951	0.474	0.857	0.628	0.737
30.0	1.974	1.722	4.532	2.657	7.928	2.23	1.946	1.505	3.169	1.62	4.128	2.054	0.724	0.701	1.76	4.8	1.127	4.207	1.051	1.942	3.59	3.348
31.0	2.006	1.788	2.366	1.04	1.154	0.945	0.819	1.235	0.982	0.951	1.229	1.309	0.859	0.998	1.022	1.573	1.07	0.459	1.312	0.693	1.061	1.046
32.0	2.188	1.87	2.038	5.504	2.078	1.82	2.569	5.427	3.343	7.664	4.119	2.364	9.641	9.787	4.669	7.592	4.633	12.287	5.953	4.489	4.183	6.462
33.0	2.791	2.001	2.592	9.832	8.317	9.944	8.932	5.676	5.977	9.819	7.225	4.145	20.631	8.919	10.448	29.745	7.043	6.303	10.042	6.821	4.208	12.781
34.0	2.817	4.506	3.573	1.729	1.459	0.797	3.765	1.465	0.446	1.395	1.655	4.61	0.959	0.554	0.883	1.912	4.834	1.08	1.206	2.193	0.594	1.309
35.0	3.103	1.438	2.886	8.53	11.826	11.294	6.161	8.117	10.838	13.016	5.476	3.089	8.541	10.501	4.398	12.214	2.673	8.846	9.83	13.537	4.025	9.162
36.0	3.121	1.907	4.295	2.402	0.679	0.671	2.84	0.363	10.579	1.051	2.773	0.792	0.43	0.128	3.968	0.729	0.931	4.493	1.688	1.023	2.591	7.51
37.0	6.784	3.038	3.287	1.466	0.919	1.167	1.577	1.388	1.633	1.222	1.43	1.422	1.497	1.468	1.456	2.178	1.727	1.334	2.164	0.971	1.366	1.476
n near Ice Core	37.0	1.0	3.0	3.0	9.0	3.0	3.0	4.0	2.0	4.0	1.0	9.0	2.0	4.0	3.0	4.0	3.0	5.0	2.0	4.0	4.0	3.0

**Figure 7.** Disagreement between each of the 17 LENS transport scenarios investigated (runs 18 through 35) and ice cores. Each model run, including individual LENS runs, the overall LENS average, as well as CMIP6, CESM2, and ice core PD/PI ratios are shown in the columns. Rows are sorted by ice core indexes defined in Figure 1. The bottom row shows the total number of ratios in each column within 0.25 of their corresponding ice cores and CESM2 ratios respectively. PD/PI ratios are color coated with the same scale defined in Figure 1 with the additional pink highlighting of ratios that fall within 0.25 of their corresponding ice core value.

### 3.5 Exact Results Depend on the Definitions of the Pre-Industrial

Previous work has shown that different definitions of the PI change the probabilities of the world meeting goals like the Paris Climate accord, specifically that the chance of exceeding 1.5°C warming by 2100 varies between 61 to 88% when the late nineteenth century's warming since the PI varies by 0.2°C (Schurer et al., 2017). However, the effect of choice of year to define the PI on wildfire baselines remains unexplored. The probability distributions in Figure 8 show that as the PI definition varies between 1750 and 1900, the median PD/PI ice core BC ratio across the 37 core dataset varies between 0.5 to 1.0 and 1.0 to 1.5 categories. Two trends are apparent as the PI definition moves closer to the PD, the relative distribution becomes narrower, indicating more constrained values, and values above 2 become more frequent. These trends are most likely dominated by the BC emission peak between 1900 and 1920 observed throughout the literature (Faïn et al., 2025; Guo et al., 2025; Hamilton et al., 2018; Liu et al., 2021; Moseid et al., 2022; Zhang et al., 2024), which raises the PI average as it increases its overlap with the peak.

Overall, results from Figure 8 confirm the idea that wildfire regimes experienced large scale changes from 1750 to 1850 due to human influences (Barker et al., 2021; Brugger et al., 2021; Chellman et al., 2017; Knorr et al., 2014; Legrand & De Angelis, 1996; McConnell et al., 2007; Thevenon et al., 2009; Whitehair et al., 2018; Whitlow et al., 1994; Zhang et al., 2024), and that different definitions of the PI within that range would represent different baseline BC radiative forcing. Although the definitions of the PD and PI do change the dataset's PD/PI ratios, changes are too small to alter any major results. Figure 5 shows minimum and maximum median ice core ratio of about 0.9 and 1.11 respectively, but corresponding model ratios are often above 2.

Aerosol radiative forcing estimates are defined in terms of the perturbation of the atmospheric energy balance due to changes in the aerosol burden from a PI baseline (IPCC,

2021). However, the PI aerosol burden is not well constrained (Carslaw et al., 2017; Mahowald et al., 2024; Robock & Graf, 1994; Wan et al., 2021), in regions where CCN are dominated by wildfire BC, PI CCN concentration uncertainty can exceed 100% of the mean (Hamilton et al., 2014) and global uncertainty in wildfire magnitude and location can alter direct aerosol and cloud albedo radiative forcing estimates by up to  $0.7 \text{ W m}^{-2}$  and  $2.4 \text{ W m}^{-2}$ , respectively (IPCC, 2021). Additionally, the chosen year that marks the beginning of the Industrial Era is important for many climate goals, such as the Paris Climate Accord, but definitions change across assessments. For example, the climate modeling community has recently adopted 1850 CE as the PI (Eyring et al., 2016), but previous work has shown that even slight variations in this year can lead to large differences in effective radiative forcing estimates, and thus, climate outcomes (Schurer et al., 2017).

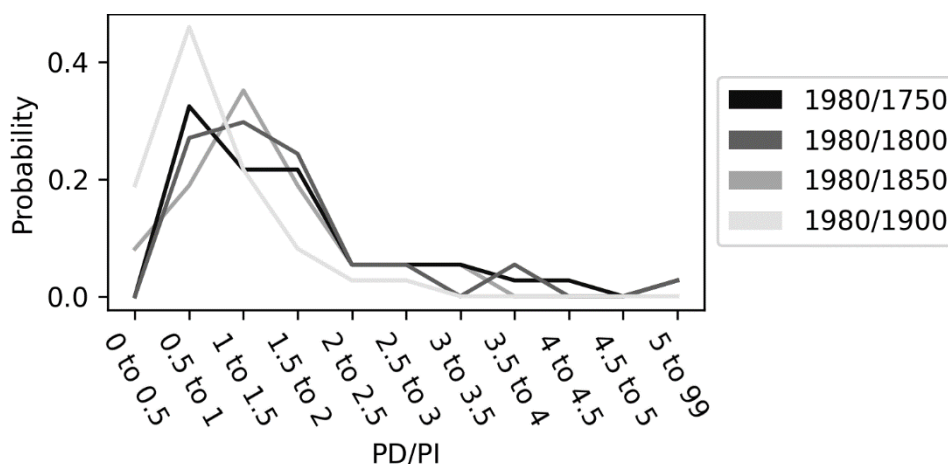


**Figure 8.** Differences in the distributions of ice core PD/PI ratios based on the definitions of the pre-industrial (PI). The PD/PI definitions differentiated in where darker colors represent an earlier definition of the PI.

## 4 SOURCES OF UNCERTAINTY

### 4.1 Deposition

To reproduce the PD to PI BC change observed in ice cores, models must accurately simulate the major processes involved in moving BC aerosol from emission source to their final ice core location. One such process is deposition, where aerosol settles out of the air onto the surface either through wet deposition, involving water, or dry deposition. Climate models parameterize these processes to make them computationally feasible, though the exact parameterization has evolved over time (Petroff & Zhang, 2010; L. Zhang et al., 2003; Leiming Zhang et al., 2001). However, adequate quantity and quality of aerosol deposition observations can be difficult to achieve on the scale needed for accurate ESM parameterization (Farmer et al., 2021). Several studies have observed deficiencies in model deposition parameterizations, including overestimates in the deposition of accumulation and Aitken mode particles and underestimates of coarse mode deposition (Emerson et al., 2020), parameterizations should account for leaf needle edge effects (Pleim et al., 2022), and 5-15% disagreements in surface fine particle concentration between models (Saylor et al., 2019). In Community Atmosphere Model version 6 (CAM6)'s Modal Aerosol Module (MAM4), BC aging has been shown to be too fast compared to experimental results and causes overestimates of surface BC concentration in some regions, a problem that could be due to miss-parameterizing SOA aging (Shen et al., 2023). One study found that adding more mechanistic dry deposition parameterizations the ModelE ESM increased its global non-dust aerosol burden by 11 to 23% from 1850 to 2000 (Clifton et al., 2024). Microphysics parameterizations can also effect atmospheric lifetime with the most pronounced effects in the polar regions (Vignati et al., 2010a). Some of these sources of uncertainty may not be evenly distributed throughout the world, where the Community

Emissions Data System (CEDDS) showed an  $R^2 = 0.73$  correlation when representing variability in surface BC in developed countries, but only a  $R^2 = 0.00019$  correlation in the global south (Ren et al., 2025).

#### 4.2 Post Deposition Processes

BC preserved in glacial ice can be dated with various methods when extracted as ice cores (S. J. Doherty et al., 2010; McConnell et al., 2007; Ming et al., 2008; Thevenon et al., 2009; Xu et al., 2009). Different types of ice core methods can quantify different groups of particles, for example, optical thermal, and chemical methods measure BC, elemental carbon (EC), and organic carbon (OC) respectively, and concentrations of each within a single sample can vary significantly. In the most extreme case, different methods can differ by over 270% when measuring the same sample (Reisinger et al., 2008). BC, EC, and sometimes OC are often interchanged, making their precise comparison of different forms of carbon in ice-cores between studies challenging (Vignati et al., 2010b). A secondary source of uncertainty in ice core BC records is dating uncertainty. Several methods exist to date ice cores, including orbital tuning (Michael L. Bender, 2002), ice accumulation modeling (Wolff et al., 2010), tie point synchronization (Svensson et al., 2020), radiometric dating (Michael L. Bender et al., 2008), annual layer counting (Maselli et al., 2013; Whitlow et al., 1992), and gas fractionation (M. L. Bender et al., 1994; Oyabu et al., 2021).

When deposition occurs over a glaciating region, BC aerosol can become trapped between snow particles and are ultimately compacted into ice. During this transition, melting, sublimation, and re-freezing of ice can redistribute BC particles vertically relative to the surrounding ice (Patrick Ginot et al., 2001; Liou et al., 2011; Schwarz et al., 2013). Multiple

studies have found that surface snow melt and runoff can increase the concentration of hydrophilic BC particles at the surface of ice cores and at the bottom of the snowpack (Sarah J. Doherty et al., 2013; P. Ginot et al., 2014; Xu et al., 2012). Under high BC concentrations, migration to the bottom of the snowpack dominates (Conway et al., 1996). Post-depositional processes can alter BC concentrations within melt seasons by between 5 and 10 times (Sarah J. Doherty et al., 2013; Xu et al., 2012), though even when significant post-depositional processes occur, temporal trends in ice core BC timeseries remain primarily driven by source emissions because vertical migration is largely limited to the uppermost layers of snow (Osmont et al., 2018). In addition to being a source of uncertainty, post-depositional processes are of interest because their redistribution of BC in snow can increase the surface albedo of ice beyond BC deposition alone (Xu et al., 2012; Yang et al., 2015). Despite the body of literature investigating post depositional processes, no CMIP6 ESM includes any post depositional processes for BC deposited to snow.

#### 4.3 Agricultural Burning

For various purposes, including field clearing, a fraction of agricultural residue, such as stalks and leaves, is burned after harvests in many regions. In some estimates, farms in regions like India burn more agricultural residue biomass than they produce in crop yields (Jethva et al., 2019). Like wildfires, agricultural burning is a source of BC, contributing an estimated 310 Gg BC per year, or 11% of global BC from biomass burning (Bond et al., 2013). Coupled with the fact that agricultural burning was present in both the PD and the PI, it is difficult to discern whether the source of PI BC comes from either wildfires or agricultural burning from ice core BC concentrations alone. Wheat, rice, and rapeseed each have been measured to have a PM<sub>2.5</sub>/BC emission ratio of 1.9, 7.3, and 0.5 for flaming combustion and 58.1, 66.3, and 47.5 for

smoldering combustion respectively (T. Zhang et al., 2015). There is a large uncertainty in the modified combustion efficiency (MCE), as well as other measures of burning completeness, in agricultural burning due to variations between plant types (Koopmans & Koppejan, 1997) and the fraction of residue burned in a given field (Venkataraman et al., 2006). Combustion efficiency and dry-matter-to-product ratios ranges of agricultural burning have been reported to be 0.68 to 0.89, and 0.71 to 0.85 respectively (Streets et al., 2003). Another source of uncertainty is temporal variability in agricultural burning. For example, from 1961 to 2011, one estimate shows that changes in agricultural burning emissions during India's green revolution increased the country's contribution to global BC forcing from 2.6% to 4.4% (X. Liu et al., 2021). Within years, BC mass concentration in North India has been shown to vary month to month and hour to hour aligned with the peak regional season and time of agricultural burning (Kharol et al., 2012; Sahu et al., 2008). Both types of these uncertainties become even larger in the PI, where data is sparser, but agricultural burning comprises a larger share of global BC emissions due to the absence of industrial emissions.

Europe is another region that performs significant agricultural burning. In 2006 agricultural burning in Eastern Europe reached Arctic glaciers, measurably reducing their albedo (Stohl et al., 2007). In the same year, agricultural burning contributed to a deterioration of air quality in Sweden (Targino et al., 2013). The ability for agricultural burning BC aerosols to reach both regions may be due to their ability to frequently pass above the boundary layer height (Amiridis et al., 2010). In general agricultural burning is estimated to account for 2.7% to 11.6% of European winter PM<sub>10</sub> (Cordell et al., 2016). To open space for agriculture and urbanization, 10-30% of Europe's forests were cleared, often using fire, between 1000 and 1800 AD (Kaplan et al., 2009, 2017). Similar land clearing came was performed in other parts of the world, but in

regions like North America, deforestation occurred mostly after 1850 (Ryan et al., 2013). The timing of Europe's land clearing can help explain why it is the region with some of the best agreement between its ice core and ESM BC ratios- because neither the post 1850 history of the region, or the ESM BC emissions dataset contain fire-based land clearing. Likewise North America shows one of the largest disagreements between models and ice core ratios and the region does have a post 1850 history of fire-based land clearing. To investigate how the inclusion of agricultural burning in models could affect their agreement with ice core observations, Hamilton et al. (2018) compared LPJ-LMfire, a model that explicitly simulates agricultural fires, to three other models that did not include agricultural fires. In comparison with ice core PD/PI ratios, LMfire performed the best out of all 4 models, supporting the notion that the omission of some agricultural fires could account for discrepancies between models and ice core observations. However, LMfire still displayed significant discrepancies with ice cores, indicating other factors are also at play (Hamilton et al., 2018).

#### 4.4 Physical Aerosol Properties

Several physical properties of BC aerosol, including particle size, as well as optical and chemical properties, can depend on the source of the aerosol (Blanco-Donado et al., 2022; L. Liu et al., 2022). Differences in these physical properties can alter aerosol transport distance (Seinfeld & Pandis, 2016). Specifically, high levels of agricultural burning can increase the fraction of accumulation mode aerosol (Sahu et al., 2008). BC emitted from the combustion of wet wood has a higher dynamic shape factor (1.8–2.17) than from dry wood (1.2–1.85) (Hu et al., 2021). Under transport in environments with high humidity or sulfuric acid concentrations, gaseous water accumulation can make BC particles more spherical (R. Zhang et al., 2008). Even for BC from a single source, such as diesel fuel, particle mobility-mass fractal dimension ( $D_{fm}$ )

can vary by over 25% (Park et al., 2003). Single Particle Soot Photometer (SP2) show responses with standard correlation factors that varied between 0.821 and 0.913 based on the source material of BC analyte (Hu et al., 2021). The results of this work indicate that the source, namely biomass burning and industrial emissions, of global BC has changed from the PI to the PD, which therefore may have affected aerosol transport and deposition location. Combustion efficiency and emission factors of a given fire vary with the specific plants that are burning (T. Zhang et al., 2015) and the amount of precipitation that has recently fallen (Röckmann et al., 2010), both of which can vary on centennial timescales (Jiménez-Moreno et al., 2008; Zuo & Qian, 2022). Significant variation in either of these factors, leading to a variation in combustion efficiency from the PI to the PD would confound BC based results since the amount of BC produced for a given unit of combusting mass would be altered. To fully address this source of uncertainty, wholistic modeling of historical meteorology and vegetation must be performed in tandem with wildfire and aerosol simulations.

#### 4.5 Reduction of Uncertainties

The analytical methodology most ice cores use to measure BC concentrations cannot be differentiated between any physical properties of BC particles that may give insight into their source type (McConnell et al., 2007). There are some studies that have used alternative methodology to study the sources of ice core records of BC. One study analyzed samples from an alpine ice core using radiometric techniques to separately quantify the amount of anthropogenic and biomass burning EC and OC (Jenk et al., 2006). They found that the fraction of anthropogenic EC and OC grew significantly from 1870 to 1980, but the results also show that the anthropogenic fraction of pre 1850 EC values are consistently near 50%, which the authors attribute to unexpected contributions from mineral dust. Another recent study used radiocarbon

analysis of an Himalayan ice core and found that the anthropogenic fraction of BC has decreased from 76 to 70% from 1990 to 2012, while the biomass burning fraction was highly correlated with South Asian wildfires (Wang et al., 2025). Despite the existence of viable techniques as shown in these two studies, to the author's knowledge, these are the only studies that have separately quantified anthropogenic and biomass burning fractions of BC in ice core records, making global analysis of trends impossible. When possible, the authors call on ice core studies to separately quantify anthropogenic and biomass burning BC aerosol in ice core records.

In summary we call for four areas of future work:

1. Inclusion of post-depositional cryosphere processes in future ESMs and how they contribute to model–observation uncertainty.
2. A reevaluation of pre-industrial to present-day fire emissions, incorporating multiple paleoenvironmental archives (van Marle et al., 2017).
3. Use ice cores records of burning in future ESM emission datasets.
4. Expand the usage of methodology to separately quantify anthropogenic and biomass burning BC aerosol in ice core records (Jenk et al., 2006; Wang et al., 2025).

## 5 CONCLUSIONS

CMIP6 models overestimate the change in BC aerosol from the PI to the PD relative to ice core observations taken in every continent, except Australia. Mean CMIP6 modeled BC ratios are outside of the first to third quartile range of corresponding ice core observations in 6/9 continental regions investigated and are significantly ( $P < 0.05$ ) larger statistically larger than ice core means globally and in 3/4 polar regions. Similar results were found for the LENS experiment and the CESM2 subset of CMIP6. Transport and other individual modeled processes

cannot fully explain this ice core – model disagreement, rather the primary source of is the emissions datasets used for biomass burning in CMIP6. These results warrant a reevaluation of the CMIP biomass burning dataset (van Marle et al., 2017), especially given the importance of PI BC aerosol baselines for upcoming radiative forcing estimates within CMIP7 and AerChemMIP2.

## 6 FUTURE WORK

Although some attempts have been made in the literature to improve ESM BC biomass burning datasets (Eckhardt et al., 2023; Guo et al., 2025; Lampe et al., 2025; Zhang et al., 2024), no study has yet integrated all available observational historical combustion proxies, including ice core BC, the charcoal record, and modern satellite and ESM data, into a single comprehensive dataset. For this reason, I plan to use the first and second chapters of my PhD to investigate the charcoal record with the intention to eventually use its data in an ESM BC emissions dataset.

Charcoal formation, known in the literature as pyrogenic carbon (PyC), is also missing in most ESMs, including the CESM2. This absence is significant because annual production of PyC is between 196 and 337 Tg C (Bowring et al., 2022; Jones et al., 2019), representing up to 16% of global total carbon emitted to the atmosphere from wildfires (Chen et al., 2023; Randerson et al., 2015). After it is formed, undisturbed pyrogenic carbon degrades to CO<sub>2</sub> with a half-life of ~100 years (Kuzyakov et al., 2014; Santos et al., 2012; Singh et al., 2012; Zimmermann et al., 2012). However, a subsequent wildfire in the vicinity will resuspend ~10% of the carbon back to the atmosphere (Bird et al., 2015; Santín et al., 2013), coupling the lifetime of pyrogenic carbon to fire frequency (Bowring et al., 2022). Specifically, if a forest with 100 Gg store of pyrogenic carbon and a present day 20-year fire return interval experiences a 50% increase in fire

occurrence by 2100 (Kloster & Lasslop, 2017) its pyrogenic carbon loss would increase by 250 Mg C/a. In the second chapter of my PhD, I plan to quantify how human and climate driven changes in fire occurrence will influence pyrogenic carbon stocks, globally and regionally within different biomes, by integrating PyC formation and degradation into the FATES vegetation component of the Community Land Model (CLM).

The third chapter of my PhD will utilize both the improved emissions dataset and the PyC-enabled version of FATES from the first and second chapters of my PhD to simulate the future trajectories of global PyC stocks under multiple climate warming scenarios. This integrated framework will enable quantitative evaluation of how future fire regimes and vegetation dynamics may alter the PyC's role in the global carbon cycle.

**REFERENCES**

- Ackerman, A. S., Toon, O. B., Stevens, D. E., Heymsfield, A. J., Ramanathan, V., & Welton, E. J. (2000). Reduction of Tropical Cloudiness by Soot. *Science*, *288*(5468), 1042–1047.  
<https://doi.org/10.1126/science.288.5468.1042>
- Andela, N., Morton, D. C., Giglio, L., Chen, Y., van der Werf, G. R., Kasibhatla, P. S., et al. (2017). A human-driven decline in global burned area. *Science*, *356*(6345), 1356–1362.  
<https://doi.org/10.1126/science.aal4108>
- Andersen, K. K., Svensson, A., Johnsen, S. J., Rasmussen, S. O., Bigler, M., Röthlisberger, R., et al. (2006). The Greenland Ice Core Chronology 2005, 15–42ka. Part 1: constructing the time scale. *Quaternary Science Reviews*, *25*(23–24), 3246–3257.  
<https://doi.org/10.1016/j.quascirev.2006.08.002>
- Andreae, M. O., & Rosenfeld, D. (2008). Aerosol–cloud–precipitation interactions. Part 1. The nature and sources of cloud-active aerosols. *Earth-Science Reviews*, *89*(1), 13–41.  
<https://doi.org/10.1016/j.earscirev.2008.03.001>
- Aragão, L. E. O. C., Anderson, L. O., Fonseca, M. G., Rosan, T. M., Vedovato, L. B., Wagner, F. H., et al. (2018). 21st Century drought-related fires counteract the decline of Amazon deforestation carbon emissions. *Nature Communications*, *9*(1), 536.  
<https://doi.org/10.1038/s41467-017-02771-y>
- Archibald, Nickless, A., Govender, N., Scholes, R. J., & Lehsten, V. (2010). Climate and the inter-annual variability of fire in southern Africa: a meta-analysis using long-term field data and satellite-derived burnt area data. *Global Ecology and Biogeography*, *19*(6), 794–809. <https://doi.org/10.1111/j.1466-8238.2010.00568.x>

- Archibald, Staver, A. C., & Levin, S. A. (2012). Evolution of human-driven fire regimes in Africa. *Proceedings of the National Academy of Sciences*, *109*(3), 847–852.  
<https://doi.org/10.1073/pnas.1118648109>
- Arora, V. K., & Melton, J. R. (2018). Reduction in global area burned and wildfire emissions since 1930s enhances carbon uptake by land. *Nature Communications*, *9*(1), 1326.  
<https://doi.org/10.1038/s41467-018-03838-0>
- Baker, J. C. A., & Spracklen, D. V. (2019). Climate Benefits of Intact Amazon Forests and the Biophysical Consequences of Disturbance. *Frontiers in Forests and Global Change*, *2*.  
<https://doi.org/10.3389/ffgc.2019.00047>
- Barker, J. D., Kaspari, S., Gabrielli, P., Wegner, A., Beaudon, E., Sierra-Hernández, M. R., & Thompson, L. (2021). Drought-induced biomass burning as a source of black carbon to the central Himalaya since 1781 CE as reconstructed from the Dasuopu ice core. *Atmospheric Chemistry and Physics*, *21*(7), 5615–5633. <https://doi.org/10.5194/acp-21-5615-2021>
- Bellouin, N., Quaas, J., Gryspeerdt, E., Kinne, S., Stier, P., Watson-Parris, D., et al. (2020). Bounding Global Aerosol Radiative Forcing of Climate Change. *Reviews of Geophysics*, *58*(1), e2019RG000660. <https://doi.org/10.1029/2019RG000660>
- Bender. (2002). Orbital tuning chronology for the Vostok climate record supported by trapped gas composition. *Earth and Planetary Science Letters*, *204*(1), 275–289.  
[https://doi.org/10.1016/S0012-821X\(02\)00980-9](https://doi.org/10.1016/S0012-821X(02)00980-9)
- Bender. (2020). Aerosol Forcing: Still Uncertain, Still Relevant. *AGU Advances*, *1*(3), e2019AV000128. <https://doi.org/10.1029/2019AV000128>

- Bender, Sowers, T., Barnola, J.-M., & Chappellaz, J. (1994). Changes in the O<sub>2</sub>/N<sub>2</sub> ratio of the atmosphere during recent decades reflected in the composition of air in the firn at Vostok Station, Antarctica. *Geophysical Research Letters*, *21*(3), 189–192.  
<https://doi.org/10.1029/93GL03548>
- Bender, Barnett, B., Dreyfus, G., Jouzel, J., & Porcelli, D. (2008). The contemporary degassing rate of <sup>40</sup>Ar from the solid Earth. *Proceedings of the National Academy of Sciences*, *105*(24), 8232–8237. <https://doi.org/10.1073/pnas.0711679105>
- Bird, M. I., Wynn, J. G., Saiz, G., Wurster, C. M., & McBeath, A. (2015). The Pyrogenic Carbon Cycle. *Annual Review of Earth and Planetary Sciences*, *43*(1), 273–298.  
<https://doi.org/10.1146/annurev-earth-060614-105038>
- Bisiaux, M. M., Edwards, R., McConnell, J. R., Curran, M. a. J., Van Ommen, T. D., Smith, A. M., et al. (2012). Changes in black carbon deposition to Antarctica from two high-resolution ice core records, 1850–2000 AD. *Atmospheric Chemistry and Physics*, *12*(9), 4107–4115. <https://doi.org/10.5194/acp-12-4107-2012>
- Boucher, O., Servonnat, J., Albright, A. L., Aumont, O., Balkanski, Y., Bastrikov, V., et al. (2020). Presentation and Evaluation of the IPSL-CM6A-LR Climate Model. *Journal of Advances in Modeling Earth Systems*, *12*(7), e2019MS002010.  
<https://doi.org/10.1029/2019MS002010>
- Bowring, S. P. K., Jones, M. W., Ciais, P., Guenet, B., & Abiven, S. (2022). Pyrogenic carbon decomposition critical to resolving fire's role in the Earth system. *Nature Geoscience*, *15*(2), 135–142. <https://doi.org/10.1038/s41561-021-00892-0>
- Browse, J., Carslaw, K. S., Arnold, S. R., Pringle, K., & Boucher, O. (2012). The scavenging processes controlling the seasonal cycle in Arctic sulphate and black carbon aerosol.

- Atmospheric Chemistry and Physics*, 12(15), 6775–6798. <https://doi.org/10.5194/acp-12-6775-2012>
- Brugger, S. O., Schwikowski, M., Gobet, E., Schwörer, C., Rohr, C., Sigl, M., et al. (2021). Alpine Glacier Reveals Ecosystem Impacts of Europe's Prosperity and Peril Over the Last Millennium. *Geophysical Research Letters*, 48(20), e2021GL095039. <https://doi.org/10.1029/2021GL095039>
- Cahoon, D. R., Stocks, B. J., Levine, J. S., Cofer, W. R., & O'Neill, K. P. (1992). Seasonal distribution of African savanna fires. *Nature*, 359(6398), 812–815. <https://doi.org/10.1038/359812a0>
- Cape, J. N., Coyle, M., & Dumitrescu, P. (2012). The atmospheric lifetime of black carbon. *Atmospheric Environment*, 59, 256–263. <https://doi.org/10.1016/j.atmosenv.2012.05.030>
- Carslaw, Lee, L. A., Reddington, C. L., Pringle, K. J., Rap, A., Forster, P. M., et al. (2013). Large contribution of natural aerosols to uncertainty in indirect forcing. *Nature*, 503(7474), 67–71. <https://doi.org/10.1038/nature12674>
- Carslaw, Gordon, H., Hamilton, D. S., Johnson, J. S., Regayre, L. A., Yoshioka, M., & Pringle, K. J. (2017). Aerosols in the Pre-industrial Atmosphere. *Current Climate Change Reports*, 3(1), 1–15. <https://doi.org/10.1007/s40641-017-0061-2>
- Chellman, N., McConnell, J. R., Arienzo, M., Pederson, G. T., Aarons, S. M., & Csank, A. (2017). Reassessment of the Upper Fremont Glacier Ice-Core Chronologies by Synchronizing of Ice-Core-Water Isotopes to a Nearby Tree-Ring Chronology. *Environmental Science & Technology*, 51(8), 4230–4238. <https://doi.org/10.1021/acs.est.6b06574>

- Chen, Y., Li, X., Xing, Y., Yan, S., Wu, D., Shi, T., et al. (2022). Historical Changes of Black Carbon in Snow and Its Radiative Forcing in CMIP6 Models. *Atmosphere*, *13*(11), 1774. <https://doi.org/10.3390/atmos13111774>
- Chen, Y., Hall, J., van Wees, D., Andela, N., Hantson, S., Giglio, L., et al. (2023). Multi-decadal trends and variability in burned area from the fifth version of the Global Fire Emissions Database (GFED5). *Earth System Science Data*, *15*(11), 5227–5259. <https://doi.org/10.5194/essd-15-5227-2023>
- Chen, Y., Xing, Y., Yan, S., Hou, Y., Li, X., Shi, T., et al. (2024). A Comprehensive Evaluation of Black Carbon in Snow and Its Radiative Forcing in CMIP5 and CMIP6 Models Based on Global Field Observations. *Journal of Geophysical Research: Atmospheres*, *129*(14), e2023JD040665. <https://doi.org/10.1029/2023JD040665>
- Clifton, O. E., Bauer, S. E., Tsigaridis, K., Aleinov, I., Cowan, T. G., Faluvegi, G., & Kelley, M. (2024). Influence of More Mechanistic Representation of Particle Dry Deposition on 1850–2000 Changes in Global Aerosol Burdens and Radiative Forcing. *Journal of Advances in Modeling Earth Systems*, *16*(3), e2023MS003952. <https://doi.org/10.1029/2023MS003952>
- Collins, W. J., Lamarque, J.-F., Schulz, M., Boucher, O., Eyring, V., Hegglin, M. I., et al. (2017). AerChemMIP: quantifying the effects of chemistry and aerosols in CMIP6. *Geoscientific Model Development*, *10*(2), 585–607. <https://doi.org/10.5194/gmd-10-585-2017>
- Conway, H., Gades, A., & Raymond, C. F. (1996). Albedo of dirty snow during conditions of melt. *Water Resources Research*, *32*(6), 1713–1718. <https://doi.org/10.1029/96WR00712>

Cozic, J., Verheggen, B., Mertes, S., Connolly, P., Bower, K., Petzold, A., et al. (2007).

Scavenging of black carbon in mixed phase clouds at the high alpine site Jungfraujoch. *Atmospheric Chemistry and Physics*, 7(7), 1797–1807. <https://doi.org/10.5194/acp-7-1797-2007>

Cozic, J., Mertes, S., Verheggen, B., Cziczo, D. J., Gallavardin, S. J., Walter, S., et al. (2008).

Black carbon enrichment in atmospheric ice particle residuals observed in lower tropospheric mixed phase clouds. *Journal of Geophysical Research: Atmospheres*, 113(D15). <https://doi.org/10.1029/2007JD009266>

Doherty, Warren, S. G., Grenfell, T. C., Clarke, A. D., & Brandt, R. E. (2010). Light-absorbing

impurities in Arctic snow. *Atmospheric Chemistry and Physics*, 10(23), 11647–11680. <https://doi.org/10.5194/acp-10-11647-2010>

Doherty, Grenfell, T. C., Forsström, S., Hegg, D. L., Brandt, R. E., & Warren, S. G. (2013).

Observed vertical redistribution of black carbon and other insoluble light-absorbing particles in melting snow. *Journal of Geophysical Research: Atmospheres*, 118(11), 5553–5569. <https://doi.org/10.1002/jgrd.50235>

Döscher, R., Acosta, M., Alessandri, A., Anthoni, P., Arsouze, T., Bergman, T., et al. (2022).

The EC-Earth3 Earth system model for the Coupled Model Intercomparison Project 6. *Geoscientific Model Development*, 15(7), 2973–3020. <https://doi.org/10.5194/gmd-15-2973-2022>

Durack, P. J., Naik, V., Nicholls, Z., O'Rourke, E., Turner, B., Buontempo, C., et al. (2025).

Earth System Forcing for CMIP7 and Beyond. <https://doi.org/10.1175/BAMS-D-25-0119.1>

- Eckhardt, S., Pisso, I., Evangeliou, N., Zwaafink, C. G., Plach, A., McConnell, J. R., et al. (2023). Revised historical Northern Hemisphere black carbon emissions based on inverse modeling of ice core records. *Nature Communications*, *14*(1), 271. <https://doi.org/10.1038/s41467-022-35660-0>
- Eichler, A., Schwikowski, M., Gäggeler, H. W., Furrer, V., Synal, H.-A., Beer, J., et al. (2000). Glaciochemical dating of an ice core from upper Grenzgletscher (4200 m a.s.l.). *Journal of Glaciology*, *46*(154), 507–515. <https://doi.org/10.3189/172756500781833098>
- Elson, P., Andrade, E. S. de, Lucas, G., May, R., Hattersley, R., Campbell, E., et al. (2024, October 8). SciTools/cartopy: REL: v0.24.1 (Version v0.24.1). Zenodo. <https://doi.org/10.5281/zenodo.13905945>
- Emerson, E. W., Hodshire, A. L., DeBolt, H. M., Bilsback, K. R., Pierce, J. R., McMeeking, G. R., & Farmer, D. K. (2020). Revisiting particle dry deposition and its role in radiative effect estimates. *Proceedings of the National Academy of Sciences*, *117*(42), 26076–26082. <https://doi.org/10.1073/pnas.2014761117>
- Extier, T., Landais, A., Bréant, C., Prié, F., Bazin, L., Dreyfus, G., et al. (2018). On the use of  $\delta^{18}\text{O}_{\text{atm}}$  for ice core dating. *Quaternary Science Reviews*, *185*, 244–257. <https://doi.org/10.1016/j.quascirev.2018.02.008>
- Eyring, V., Bony, S., Meehl, G. A., Senior, C. A., Stevens, B., Stouffer, R. J., & Taylor, K. E. (2016). Overview of the Coupled Model Intercomparison Project Phase 6 (CMIP6) experimental design and organization. *Geoscientific Model Development*, *9*(5), 1937–1958. <https://doi.org/10.5194/gmd-9-1937-2016>
- Faïn, X., Szopa, S., Naïk, V., Martinerie, P., Etheridge, D. M., Rhodes, R. H., et al. (2025). Preindustrial-to-present-day changes in atmospheric carbon monoxide: agreement and

- gaps between ice archives and global model reconstructions. *Atmospheric Chemistry and Physics*, 25(2), 1105–1119. <https://doi.org/10.5194/acp-25-1105-2025>
- Farmer, D. K., Boedicker, E. K., & DeBolt, H. M. (2021). Dry Deposition of Atmospheric Aerosols: Approaches, Observations, and Mechanisms. *Annual Review of Physical Chemistry*, 72(Volume 72, 2021), 375–397. <https://doi.org/10.1146/annurev-physchem-090519-034936>
- Foley, J. A., DeFries, R., Asner, G. P., Barford, C., Bonan, G., Carpenter, S. R., et al. (2005). Global Consequences of Land Use. *Science*, 309(5734), 570–574. <https://doi.org/10.1126/science.1111772>
- Gabbi, J., Huss, M., Bauder, A., Cao, F., & Schwikowski, M. (2015). The impact of Saharan dust and black carbon on albedo and long-term mass balance of an Alpine glacier. *The Cryosphere*, 9(4), 1385–1400. <https://doi.org/10.5194/tc-9-1385-2015>
- Giglio, L., Boschetti, L., Roy, D. P., Humber, M. L., & Justice, C. O. (2018). The Collection 6 MODIS burned area mapping algorithm and product. *Remote Sensing of Environment*, 217, 72–85. <https://doi.org/10.1016/j.rse.2018.08.005>
- Ginot, P., Dumont, M., Lim, S., Patris, N., Taupin, J.-D., Wagnon, P., et al. (2014). A 10 year record of black carbon and dust from a Mera Peak ice core (Nepal): variability and potential impact on melting of Himalayan glaciers. *The Cryosphere*, 8(4), 1479–1496. <https://doi.org/10.5194/tc-8-1479-2014>
- Ginot, Patrick, Kull, C., Schwikowski, M., Schotterer, U., & Gäggeler, H. W. (2001). Effects of postdepositional processes on snow composition of a subtropical glacier (Cerro Tapado, Chilean Andes). *Journal of Geophysical Research: Atmospheres*, 106(D23), 32375–32386. <https://doi.org/10.1029/2000JD000071>

- Goldewijk, K. K. (2005). Three Centuries of Global Population Growth: A Spatial Referenced Population (Density) Database for 1700–2000. *Population and Environment*, 26(4), 343–367. <https://doi.org/10.1007/s11111-005-3346-7>
- Guo, Z., Li, W., Ciais, P., Sitch, S., van der Werf, G. R., Bowring, S. P. K., et al. (2025). Reconstructed global monthly burned area maps from 1901 to 2020. *Earth System Science Data Discussions*, 1–28. <https://doi.org/10.5194/essd-2024-556>
- Hadley, O. L., & Kirchstetter, T. W. (2012). Black-carbon reduction of snow albedo. *Nature Climate Change*, 2(6), 437–440. <https://doi.org/10.1038/nclimate1433>
- Hamilton, Lee, L. A., Pringle, K. J., Reddington, C. L., Spracklen, D. V., & Carslaw, K. S. (2014). Occurrence of pristine aerosol environments on a polluted planet. *Proceedings of the National Academy of Sciences*, 111(52), 18466–18471. <https://doi.org/10.1073/pnas.1415440111>
- Hamilton, Hantson, S., Scott, C. E., Kaplan, J. O., Pringle, K. J., Nieradzik, L. P., et al. (2018). Reassessment of pre-industrial fire emissions strongly affects anthropogenic aerosol forcing. *Nature Communications*, 9(1), 3182. <https://doi.org/10.1038/s41467-018-05592-9>
- Hansen, J., & Nazarenko, L. (2004). Soot climate forcing via snow and ice albedos. *Proceedings of the National Academy of Sciences*, 101(2), 423–428. <https://doi.org/10.1073/pnas.2237157100>
- Harris, C. R., Millman, K. J., van der Walt, S. J., Gommers, R., Virtanen, P., Cournapeau, D., et al. (2020). Array programming with NumPy. *Nature*, 585(7825), 357–362. <https://doi.org/10.1038/s41586-020-2649-2>

- Hoesly, R. M., Smith, S. J., Feng, L., Klimont, Z., Janssens-Maenhout, G., Pitkanen, T., et al. (2018). Historical (1750–2014) anthropogenic emissions of reactive gases and aerosols from the Community Emissions Data System (CEDS). *Geoscientific Model Development*, *11*(1), 369–408. <https://doi.org/10.5194/gmd-11-369-2018>
- Hunter, J. D. (2007). Matplotlib: A 2D Graphics Environment. *Computing in Science & Engineering*, *9*(3), 90–95. <https://doi.org/10.1109/MCSE.2007.55>
- van den Hurk, B., Kim, H., Krinner, G., Seneviratne, S. I., Derksen, C., Oki, T., et al. (2016). LS3MIP (v1.0) contribution to CMIP6: the Land Surface, Snow and Soil moisture Model Intercomparison Project – aims, setup and expected outcome. *Geoscientific Model Development*, *9*(8), 2809–2832. <https://doi.org/10.5194/gmd-9-2809-2016>
- IPCC. (2021). *Climate Change 2021: The Physical Science Basis. Contribution of Working Group I to the Sixth Assessment Report of the Intergovernmental Panel on Climate Change* (Vol. In Press). Cambridge, United Kingdom and New York, NY, USA: Cambridge University Press. <https://doi.org/10.1017/9781009157896>
- Jacobson, M. Z. (2004). Climate response of fossil fuel and biofuel soot, accounting for soot's feedback to snow and sea ice albedo and emissivity. *Journal of Geophysical Research: Atmospheres*, *109*(D21). <https://doi.org/10.1029/2004JD004945>
- Jones, M. W., Santín, C., van der Werf, G. R., & Doerr, S. H. (2019). Global fire emissions buffered by the production of pyrogenic carbon. *Nature Geoscience*, *12*(9), 742–747. <https://doi.org/10.1038/s41561-019-0403-x>
- Jones, M. W., Abatzoglou, J. T., Veraverbeke, S., Andela, N., Lasslop, G., Forkel, M., et al. (2022). Global and Regional Trends and Drivers of Fire Under Climate Change. *Reviews of Geophysics*, *60*(3), e2020RG000726. <https://doi.org/10.1029/2020RG000726>

- Kang, S., Zhang, Y., Qian, Y., & Wang, H. (2020). A review of black carbon in snow and ice and its impact on the cryosphere. *Earth-Science Reviews*, 210, 103346.  
<https://doi.org/10.1016/j.earscirev.2020.103346>
- Kaplan, J. O., Krumhardt, K. M., Gaillard, M.-J., Sugita, S., Trondman, A.-K., Fyfe, R., et al. (2017). Constraining the Deforestation History of Europe: Evaluation of Historical Land Use Scenarios with Pollen-Based Land Cover Reconstructions. *Land*, 6(4), 91.  
<https://doi.org/10.3390/land6040091>
- Kawamiya, M., Hajima, T., Tachiiri, K., Watanabe, S., & Yokohata, T. (2020). Two decades of Earth system modeling with an emphasis on Model for Interdisciplinary Research on Climate (MIROC). *Progress in Earth and Planetary Science*, 7(1), 64.  
<https://doi.org/10.1186/s40645-020-00369-5>
- Kay, J. E., Deser, C., Phillips, A., Mai, A., Hannay, C., Strand, G., et al. (2015). The Community Earth System Model (CESM) Large Ensemble Project: A Community Resource for Studying Climate Change in the Presence of Internal Climate Variability.  
<https://doi.org/10.1175/BAMS-D-13-00255.1>
- Kelley, D. I., Bistinas, I., Whitley, R., Burton, C., Marthews, T. R., & Dong, N. (2019). How contemporary bioclimatic and human controls change global fire regimes. *Nature Climate Change*, 9(9), 690–696. <https://doi.org/10.1038/s41558-019-0540-7>
- Kloster, S., & Lasslop, G. (2017). Historical and future fire occurrence (1850 to 2100) simulated in CMIP5 Earth System Models. *Global and Planetary Change*, 150, 58–69.  
<https://doi.org/10.1016/j.gloplacha.2016.12.017>

- Knorr, W., Kaminski, T., Arneth, A., & Weber, U. (2014). Impact of human population density on fire frequency at the global scale. *Biogeosciences*, *11*(4), 1085–1102.  
<https://doi.org/10.5194/bg-11-1085-2014>
- Koch, D., & Del Genio, A. D. (2010). Black carbon semi-direct effects on cloud cover: review and synthesis. *Atmospheric Chemistry and Physics*, *10*(16), 7685–7696.  
<https://doi.org/10.5194/acp-10-7685-2010>
- Kuzyakov, Y., Bogomolova, I., & Glaser, B. (2014). Biochar stability in soil: Decomposition during eight years and transformation as assessed by compound-specific <sup>14</sup>C analysis. *Soil Biology and Biochemistry*, *70*, 229–236.  
<https://doi.org/10.1016/j.soilbio.2013.12.021>
- Lamarque, J.-F., Shindell, D. T., Josse, B., Young, P. J., Cionni, I., Eyring, V., et al. (2013). The Atmospheric Chemistry and Climate Model Intercomparison Project (ACCMIP): overview and description of models, simulations and climate diagnostics. *Geoscientific Model Development*, *6*(1), 179–206. <https://doi.org/10.5194/gmd-6-179-2013>
- Lampe, S., Gudmundsson, L., Kraft, B., Hantson, S., Kelley, D., Humphrey, V., et al. (2025). BuRNN (v1.0): A Data-Driven Fire Model. *EGUsphere*, 1–45.  
<https://doi.org/10.5194/egusphere-2025-3550>
- Lee, Y. H., Lamarque, J.-F., Flanner, M. G., Jiao, C., Shindell, D. T., Berntsen, T., et al. (2013). Evaluation of preindustrial to present-day black carbon and its albedo forcing from Atmospheric Chemistry and Climate Model Intercomparison Project (ACCMIP). *Atmospheric Chemistry and Physics*, *13*(5), 2607–2634. <https://doi.org/10.5194/acp-13-2607-2013>

- Legrand, M., & De Angelis, M. (1996). Light carboxylic acids in Greenland ice: A record of past forest fires and vegetation emissions from the boreal zone. *Journal of Geophysical Research: Atmospheres*, *101*(D2), 4129–4145. <https://doi.org/10.1029/95JD03296>
- Li, Y., & Flanner, M. G. (2018). Investigating the impact of aerosol deposition on snowmelt over the Greenland Ice Sheet using a large-ensemble kernel. *Atmospheric Chemistry and Physics*, *18*(21), 16005–16018. <https://doi.org/10.5194/acp-18-16005-2018>
- Liefeld, J. (2025, June 23). InterpolateScalingPy (Version 1.0). Retrieved from <https://doi.org/10.5281/zenodo.15733193>
- Liou, K. N., Takano, Y., & Yang, P. (2011). Light absorption and scattering by aggregates: Application to black carbon and snow grains. *Journal of Quantitative Spectroscopy and Radiative Transfer*, *112*(10), 1581–1594. <https://doi.org/10.1016/j.jqsrt.2011.03.007>
- Liu, He, C., Schwarz, J. P., & Wang, X. (2020). Lifecycle of light-absorbing carbonaceous aerosols in the atmosphere. *Npj Climate and Atmospheric Science*, *3*(1), 1–18. <https://doi.org/10.1038/s41612-020-00145-8>
- Liu, Kaplan, J. O., Mickley, L. J., Li, Y., Chellman, N. J., Arienzo, M. M., et al. (2021). Improved estimates of preindustrial biomass burning reduce the magnitude of aerosol climate forcing in the Southern Hemisphere. *Science Advances*, *7*(22), eabc1379. <https://doi.org/10.1126/sciadv.abc1379>
- Ma, X., & Wang, A. (2024). Evaluation and Uncertainty Analysis of the Land Surface Hydrology in LS3MIP Models Over China. *Earth and Space Science*, *11*(7), e2023EA003391. <https://doi.org/10.1029/2023EA003391>

- Mahowald, N. M., Li, L., Albani, S., Hamilton, D. S., & Kok, J. F. (2024). Opinion: The importance of historical and paleoclimate aerosol radiative effects. *Atmospheric Chemistry and Physics*, 24(1), 533–551. <https://doi.org/10.5194/acp-24-533-2024>
- van Marle, M. J. E., Kloster, S., Magi, B. I., Marlon, J. R., Daniau, A.-L., Field, R. D., et al. (2017). Historic global biomass burning emissions for CMIP6 (BB4CMIP) based on merging satellite observations with proxies and fire models (1750–2015). *Geoscientific Model Development*, 10(9), 3329–3357. <https://doi.org/10.5194/gmd-10-3329-2017>
- Marlon, J. R., Bartlein, P. J., Carcaillet, C., Gavin, D. G., Harrison, S. P., Higuera, P. E., et al. (2008). Climate and human influences on global biomass burning over the past two millennia. *Nature Geoscience*, 1(10), 697–702. <https://doi.org/10.1038/ngeo313>
- Maselli, O. J., Fritzsche, D., Diedrich, Layman, Lawrence, McConnell, Joseph R., & Meyer, H. (2013). Comparison of water isotope-ratio determinations using two cavity ring-down instruments and classical mass spectrometry in continuous ice-core analysis. *Isotopes in Environmental and Health Studies*, 49(3), 387–398. <https://doi.org/10.1080/10256016.2013.781598>
- McConnell, J. R. (2010). New Directions: Historical black carbon and other ice core aerosol records in the Arctic for GCM evaluation. *Atmospheric Environment*, 44(21), 2665–2666. <https://doi.org/10.1016/j.atmosenv.2010.04.004>
- McConnell, J. R., Edwards, R., Kok, G. L., Flanner, M. G., Zender, C. S., Saltzman, E. S., et al. (2007). 20th-Century Industrial Black Carbon Emissions Altered Arctic Climate Forcing. *Science*, 317(5843), 1381–1384. <https://doi.org/10.1126/science.1144856>

- Ming, J., Cachier, H., Xiao, C., Qin, D., Kang, S., Hou, S., & Xu, J. (2008). Black carbon record based on a shallow Himalayan ice core and its climatic implications. *Atmospheric Chemistry and Physics*, 8(5), 1343–1352. <https://doi.org/10.5194/acp-8-1343-2008>
- Mollicone, D., Eva, H. D., & Achard, F. (2006). Human role in Russian wild fires. *Nature*, 440(7083), 436–437. <https://doi.org/10.1038/440436a>
- Moseid, K. O., Schulz, M., Eichler, A., Schwikowski, M., McConnell, J. R., Olivié, D., et al. (2022). Using Ice Cores to Evaluate CMIP6 Aerosol Concentrations Over the Historical Era. *Journal of Geophysical Research: Atmospheres*, 127(18). <https://doi.org/10.1029/2021JD036105>
- Nikonovas, T., Spessa, A., Doerr, S. H., Clay, G. D., & Mezbahuddin, S. (2020). Near-complete loss of fire-resistant primary tropical forest cover in Sumatra and Kalimantan. *Communications Earth & Environment*, 1(1), 65. <https://doi.org/10.1038/s43247-020-00069-4>
- Osmont, D., Wendl, I. A., Schmidely, L., Sigl, M., Vega, C. P., Isaksson, E., & Schwikowski, M. (2018). An 800-year high-resolution black carbon ice core record from Lomonosovfonna, Svalbard. *Atmospheric Chemistry and Physics*, 18(17), 12777–12795. <https://doi.org/10.5194/acp-18-12777-2018>
- Oyabu, I., Kawamura, K., Uchida, T., Fujita, S., Kitamura, K., Hirabayashi, M., et al. (2021). Fractionation of O<sub>2</sub>/N<sub>2</sub> and Ar/N<sub>2</sub> in the Antarctic ice sheet during bubble formation and bubble–clathrate hydrate transition from precise gas measurements of the Dome Fuji ice core. *The Cryosphere*, 15(12), 5529–5555. <https://doi.org/10.5194/tc-15-5529-2021>
- Pausas, J. G., & Keeley, J. E. (2014). Abrupt Climate-Independent Fire Regime Changes. *Ecosystems*, 17(6), 1109–1120. <https://doi.org/10.1007/s10021-014-9773-5>

- Pechony, O., & Shindell, D. T. (2010). Driving forces of global wildfires over the past millennium and the forthcoming century. *Proceedings of the National Academy of Sciences*, *107*(45), 19167–19170. <https://doi.org/10.1073/pnas.1003669107>
- Petroff, A., & Zhang, L. (2010). Development and validation of a size-resolved particle dry deposition scheme for application in aerosol transport models. *Geoscientific Model Development*, *3*(2), 753–769. <https://doi.org/10.5194/gmd-3-753-2010>
- Pleim, J. E., Ran, L., Saylor, R. D., Willison, J., & Binkowski, F. S. (2022). A New Aerosol Dry Deposition Model for Air Quality and Climate Modeling. *Journal of Advances in Modeling Earth Systems*, *14*(11), e2022MS003050. <https://doi.org/10.1029/2022MS003050>
- Rabin, S. S., Melton, J. R., Lasslop, G., Bachelet, D., Forrest, M., Hantson, S., et al. (2017). The Fire Modeling Intercomparison Project (FireMIP), phase 1: experimental and analytical protocols with detailed model descriptions. *Geoscientific Model Development*, *10*(3), 1175–1197. <https://doi.org/10.5194/gmd-10-1175-2017>
- Randerson, van der Werf, Giglio, Collatz, & Kasibhatla. (2015). Global Fire Emissions Database, Version 4.1 (GFEDv4) | NASA Earthdata [Data set]. Earth Science Data Systems, NASA. Retrieved from <https://www.earthdata.nasa.gov/data/catalog/ornl-cloud-fire-emissions-v4-r1-1293-4.1>
- Reisinger, P., Wonaschütz, A., Hitzenberger, R., Petzold, A., Bauer, H., Jankowski, N., et al. (2008). Intercomparison of Measurement Techniques for Black or Elemental Carbon Under Urban Background Conditions in Wintertime: Influence of Biomass Combustion. *Environmental Science & Technology*, *42*(3), 884–889. <https://doi.org/10.1021/es0715041>

- Ren, Y., Oxford, C., Zhang, D., Liu, X., Zhu, H., Dillner, A., et al. (2025, February 17). Black Carbon Emissions Generally Underestimated in the Global South as Revealed by Globally Distributed Measurements. Research Square. <https://doi.org/10.21203/rs.3.rs-6024974/v1>
- Robock, A., & Graf, H.-F. (1994). Effects of pre-industrial human activities on climate. *Chemosphere*, 29(5), 1087–1097. [https://doi.org/10.1016/0045-6535\(94\)90169-4](https://doi.org/10.1016/0045-6535(94)90169-4)
- Roehrig, R., Beau, I., Saint-Martin, D., Alias, A., Decharme, B., Guérémy, J.-F., et al. (2020). The CNRM Global Atmosphere Model ARPEGE-Climat 6.3: Description and Evaluation. *Journal of Advances in Modeling Earth Systems*, 12(7), e2020MS002075. <https://doi.org/10.1029/2020MS002075>
- Rowlinson, M. J., Rap, A., Hamilton, D. S., Pope, R. J., Hantson, S., Arnold, S. R., et al. (2020). Tropospheric ozone radiative forcing uncertainty due to pre-industrial fire and biogenic emissions. *Atmospheric Chemistry and Physics*, 20(18), 10937–10951. <https://doi.org/10.5194/acp-20-10937-2020>
- Rudel, T. K., Defries, R., Asner, G. P., & Laurance, W. F. (2009). Changing Drivers of Deforestation and New Opportunities for Conservation. *Conservation Biology*, 23(6), 1396–1405. <https://doi.org/10.1111/j.1523-1739.2009.01332.x>
- Ryan, K. C., Knapp, E. E., & Varner, J. M. (2013). Prescribed fire in North American forests and woodlands: history, current practice, and challenges. *Frontiers in Ecology and the Environment*, 11(s1), e15–e24. <https://doi.org/10.1890/120329>
- Santín, C., Doerr, S. H., Preston, C., & Bryant, R. (2013). Consumption of residual pyrogenic carbon by wildfire. *International Journal of Wildland Fire*, 22(8), 1072–1077. <https://doi.org/10.1071/WF12190>

- Santos, F., Torn, M. S., & Bird, J. A. (2012). Biological degradation of pyrogenic organic matter in temperate forest soils. *Soil Biology and Biochemistry*, *51*, 115–124.  
<https://doi.org/10.1016/j.soilbio.2012.04.005>
- Saylor, R. D., Baker, Barry D., Lee, Pius, Tong, Daniel, Pan, Li, & Hicks, B. B. (2019). The particle dry deposition component of total deposition from air quality models: right, wrong or uncertain? *Tellus B: Chemical and Physical Meteorology*, *71*(1), 1550324.  
<https://doi.org/10.1080/16000889.2018.1550324>
- Schmitt, C. G., Riggs, B. L., Horodyskyj, U. N., Khan, A. L., Ewing, H. A., All, J. D., & Sanchez Rodriguez, W. (2019). The measurement and impact of light absorbing particles on snow surfaces. *The Cryosphere Discussions*, 1–16. <https://doi.org/10.5194/tc-2019-162>
- Schulzweida, U. (2023). CDO User Guide. <https://doi.org/10.5281/zenodo.10020800>
- Schurer, A. P., Mann, M. E., Hawkins, E., Tett, S. F. B., & Hegerl, G. C. (2017). Importance of the pre-industrial baseline for likelihood of exceeding Paris goals. *Nature Climate Change*, *7*(8), 563–567. <https://doi.org/10.1038/nclimate3345>
- Schwarz, J. P., Gao, R. S., Perring, A. E., Spackman, J. R., & Fahey, D. W. (2013). Black carbon aerosol size in snow. *Scientific Reports*, *3*(1), 1356. <https://doi.org/10.1038/srep01356>
- Seinfeld, J., & Pandis, S. (2016). *Atmospheric Chemistry and Physics: From Air Pollution to Climate Change, 3rd Edition* | Wiley (3rd ed.). Wiley. Retrieved from <https://www.wiley.com/en-us/Atmospheric+Chemistry+and+Physics%3A+From+Air+Pollution+to+Climate+Change%2C+3rd+Edition-p-9781118947401>

- Shen, W., Wang, M., Liu, Y., Dong, X., Zhao, D., Yue, M., et al. (2023). Evaluating BC Aging Processes in the Community Atmosphere Model Version 6 (CAM6). *Journal of Geophysical Research: Atmospheres*, 128(3), e2022JD037427.  
<https://doi.org/10.1029/2022JD037427>
- Simpkins, G. (2018). Aerosol–cloud interactions. *Nature Climate Change*, 8(6), 457–457.  
<https://doi.org/10.1038/s41558-018-0195-9>
- Singh, B. P., Cowie, A. L., & Smernik, R. J. (2012). Biochar Carbon Stability in a Clayey Soil As a Function of Feedstock and Pyrolysis Temperature. *Environmental Science & Technology*, 46(21), 11770–11778. <https://doi.org/10.1021/es302545b>
- Staal, A., Tuinenburg, O. A., Bosmans, J. H. C., Holmgren, M., van Nes, E. H., Scheffer, M., et al. (2018). Forest-rainfall cascades buffer against drought across the Amazon. *Nature Climate Change*, 8(6), 539–543. <https://doi.org/10.1038/s41558-018-0177-y>
- Stohl, A. (2006). Characteristics of atmospheric transport into the Arctic troposphere. *Journal of Geophysical Research: Atmospheres*, 111(D11). <https://doi.org/10.1029/2005JD006888>
- Stohl, A., & Sodemann, H. (2010). Characteristics of atmospheric transport into the Antarctic troposphere. *Journal of Geophysical Research: Atmospheres*, 115(D2).  
<https://doi.org/10.1029/2009JD012536>
- Svensson, A., Dahl-Jensen, D., Steffensen, J. P., Blunier, T., Rasmussen, S. O., Vinther, B. M., et al. (2020). Bipolar volcanic synchronization of abrupt climate change in Greenland and Antarctic ice cores during the last glacial period. *Climate of the Past*, 16(4), 1565–1580.  
<https://doi.org/10.5194/cp-16-1565-2020>

- Swart, N. C., Cole, J. N. S., Kharin, V. V., Lazare, M., Scinocca, J. F., Gillett, N. P., et al. (2019). The Canadian Earth System Model version 5 (CanESM5.0.3). *Geoscientific Model Development*, 12(11), 4823–4873. <https://doi.org/10.5194/gmd-12-4823-2019>
- Thevenon, F., Anselmetti, F. S., Bernasconi, S. M., & Schwikowski, M. (2009). Mineral dust and elemental black carbon records from an Alpine ice core (Colle Gnifetti glacier) over the last millennium. *Journal of Geophysical Research: Atmospheres*, 114(D17). <https://doi.org/10.1029/2008JD011490>
- Vignati, E., Karl, M., Krol, M., Wilson, J., Stier, P., & Cavalli, F. (2010a). Sources of uncertainties in modelling black carbon at the global scale. *Atmospheric Chemistry and Physics*, 10(6), 2595–2611. <https://doi.org/10.5194/acp-10-2595-2010>
- Vignati, E., Karl, M., Krol, M., Wilson, J., Stier, P., & Cavalli, F. (2010b). Sources of uncertainties in modelling black carbon at the global scale. *Atmospheric Chemistry and Physics*, 10(6), 2595–2611. <https://doi.org/10.5194/acp-10-2595-2010>
- Virtanen, P., Gommers, R., Oliphant, T. E., Haberland, M., Reddy, T., Cournapeau, D., et al. (2020). SciPy 1.0: fundamental algorithms for scientific computing in Python. *Nature Methods*, 17(3), 261–272. <https://doi.org/10.1038/s41592-019-0686-2>
- Wan, J. S., Hamilton, D. S., & Mahowald, N. M. (2021). Importance of Uncertainties in the Spatial Distribution of Preindustrial Wildfires for Estimating Aerosol Radiative Forcing. *Geophysical Research Letters*, 48(6), e2020GL089758. <https://doi.org/10.1029/2020GL089758>
- Ward, J. L., Flanner, M. G., Bergin, M., Dibb, J. E., Polashenski, C. M., Soja, A. J., & Thomas, J. L. (2018). Modeled Response of Greenland Snowmelt to the Presence of Biomass Burning-Based Absorbing Aerosols in the Atmosphere and Snow. *Journal of*

- Geophysical Research: Atmospheres*, 123(11), 6122–6141.  
<https://doi.org/10.1029/2017JD027878>
- van der Werf, G. R., Randerson, J. T., Giglio, L., van Leeuwen, T. T., Chen, Y., Rogers, B. M., et al. (2017). Global fire emissions estimates during 1997–2016. *Earth System Science Data*, 9(2), 697–720. <https://doi.org/10.5194/essd-9-697-2017>
- Whitehair, L., Fulé, P. Z., Meador, A. S., Azpeleta Tarancón, A., & Kim, Y. (2018). Fire regime on a cultural landscape: Navajo Nation. *Ecology and Evolution*, 8(19), 9848–9858.  
<https://doi.org/10.1002/ece3.4470>
- Whitlow, S., Mayewski, P. A., & Dibb, J. E. (1992). A comparison of major chemical species seasonal concentration and accumulation at the South Pole and summit, Greenland. *Atmospheric Environment. Part A. General Topics*, 26(11), 2045–2054.  
[https://doi.org/10.1016/0960-1686\(92\)90089-4](https://doi.org/10.1016/0960-1686(92)90089-4)
- Whitlow, S., Mayewski, P., Dibb, J., Holdsworth, G., & Twickler, M. (1994). An ice-core-based record of biomass burning in the Arctic and Subarctic, 1750–1980. *Tellus B*, 46(3), 234–242. <https://doi.org/10.1034/j.1600-0889.1994.t01-2-00006.x>
- Wolff, E. W., Chappellaz, J., Blunier, T., Rasmussen, S. O., & Svensson, A. (2010). Millennial-scale variability during the last glacial: The ice core record. *Quaternary Science Reviews*, 29(21–22), 2828–2838. <https://doi.org/10.1016/j.quascirev.2009.10.013>
- Xu, B., Cao, J., Hansen, J., Yao, T., Joswita, D. R., Wang, N., et al. (2009). Black soot and the survival of Tibetan glaciers. *Proceedings of the National Academy of Sciences*, 106(52), 22114–22118. <https://doi.org/10.1073/pnas.0910444106>

- Xu, B., Cao, J., Joswiak, D. R., Liu, X., Zhao, H., & He, J. (2012). Post-depositional enrichment of black soot in snow-pack and accelerated melting of Tibetan glaciers. *Environmental Research Letters*, 7(1), 014022. <https://doi.org/10.1088/1748-9326/7/1/014022>
- Yang, S., Xu, B., Cao, J., Zender, C. S., & Wang, M. (2015). Climate effect of black carbon aerosol in a Tibetan Plateau glacier. *Atmospheric Environment*, 111, 71–78. <https://doi.org/10.1016/j.atmosenv.2015.03.016>
- Yukimoto, S., Kawai, H., Koshiro, T., Oshima, N., Yoshida, K., Urakawa, S., et al. (2019). The Meteorological Research Institute Earth System Model Version 2.0, MRI-ESM2.0: Description and Basic Evaluation of the Physical Component. *Journal of the Meteorological Society of Japan. Ser. II*, 97(5), 931–965. <https://doi.org/10.2151/jmsj.2019-051>
- Zender, C. S. (2008). Analysis of self-describing gridded geoscience data with netCDF Operators (NCO). *Environmental Modelling & Software*, 23(10), 1338–1342. <https://doi.org/10.1016/j.envsoft.2008.03.004>
- Zhang, Gong, S., Padro, J., & Barrie, L. (2001). A size-segregated particle dry deposition scheme for an atmospheric aerosol module. *Atmospheric Environment*, 35(3), 549–560. [https://doi.org/10.1016/S1352-2310\(00\)00326-5](https://doi.org/10.1016/S1352-2310(00)00326-5)
- Zhang, Brook, J. R., & Vet, R. (2003). A revised parameterization for gaseous dry deposition in air-quality models. *Atmospheric Chemistry and Physics*, 3(6), 2067–2082. <https://doi.org/10.5194/acp-3-2067-2003>
- Zhang, Zhang, F., Zhang, G., & Yan, W. (2022). Why Do CMIP6 Models Fail to Simulate Snow Depth in Terms of Temporal Change and High Mountain Snow of China Skillfully?

*Geophysical Research Letters*, 49(15), e2022GL098888.

<https://doi.org/10.1029/2022GL098888>

Zhang, Chellman, N. J., Kaplan, J. O., Mickley, L. J., Ito, T., Wang, X., et al. (2024). Improved biomass burning emissions from 1750 to 2010 using ice core records and inverse modeling. *Nature Communications*, 15(1), 3651. <https://doi.org/10.1038/s41467-024-47864-7>

Zimmermann, M., Bird, M. I., Wurster, C., Saiz, G., Goodrick, I., Barta, J., et al. (2012). Rapid degradation of pyrogenic carbon. *Global Change Biology*, 18(11), 3306–3316.

<https://doi.org/10.1111/j.1365-2486.2012.02796.x>

**APPENDICES**

## Appendix A

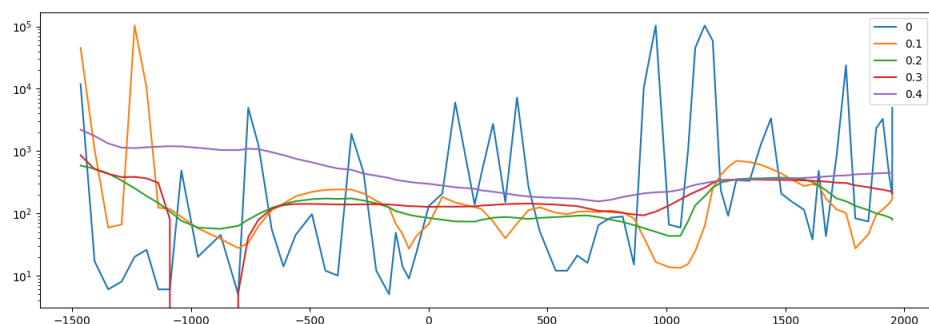


**Figure A1.** Kilimanjaro levoglucosan ice core (Core 9) log scale timeseries smoothed with different lowess smoothing parameters.

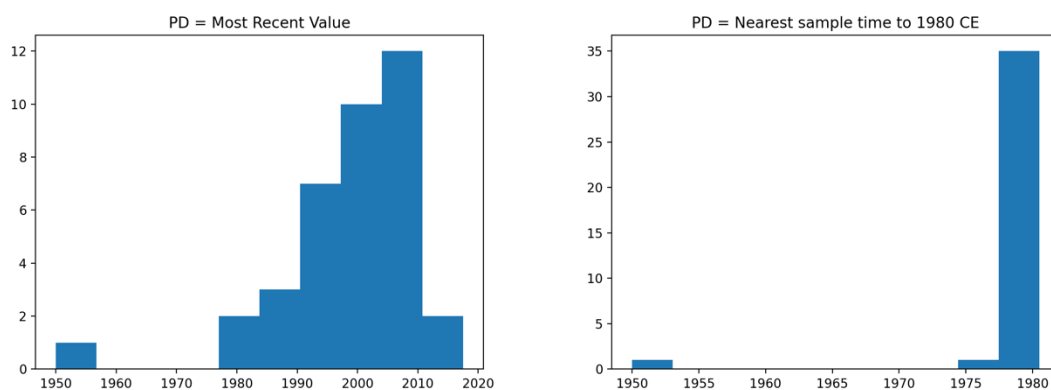


**Figure A2.** Histograms of each ice core's PD value using two different definitions: most recent value (left) and nearest sample date to 1980 CE (right). The PD year mean, standard deviation, and range were 1998.6, 12.3, and 67.5 for the most recent approach, and 1979.0, 4.92, and 30.5 for the 1980 approach respectively.

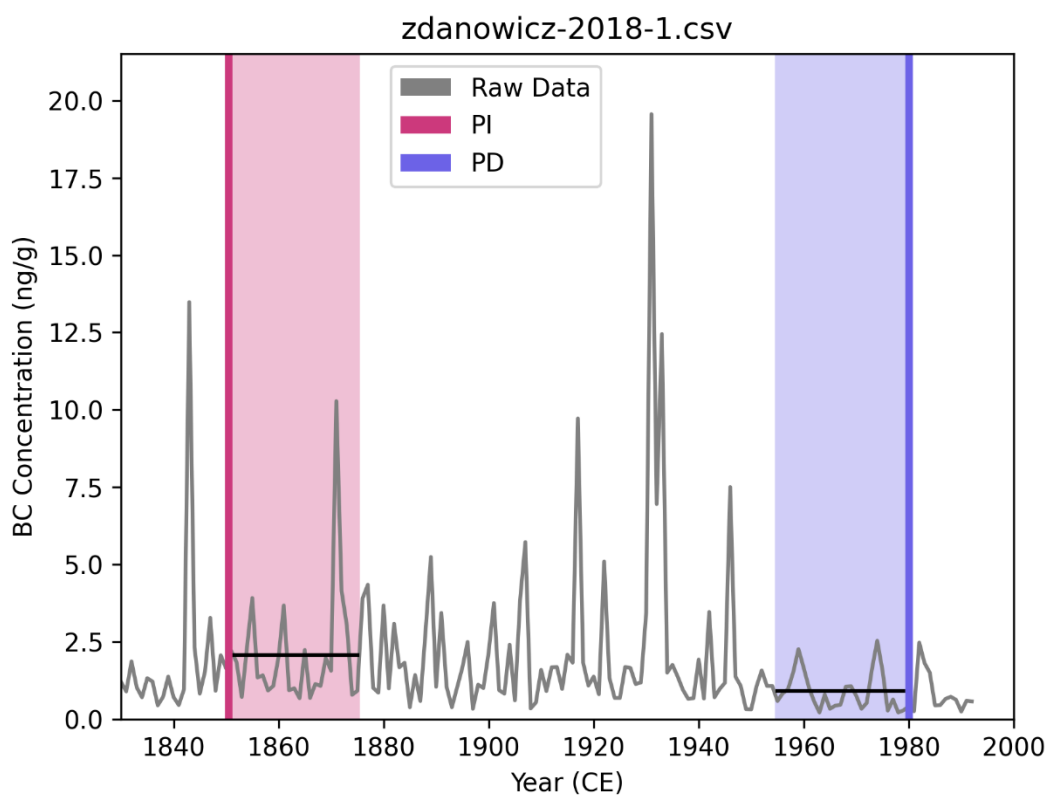


**Figure A3.** Example of methodology applied to each ice core. First the data with the nearest dates to 1850 and 1980 are found (thick pink and blue lines) then the 25 years of data shown in light pink and light blue are averaged to produce the BC values for PI and PD. Finally, these two numbers are divided to get the PD/PI ratio.

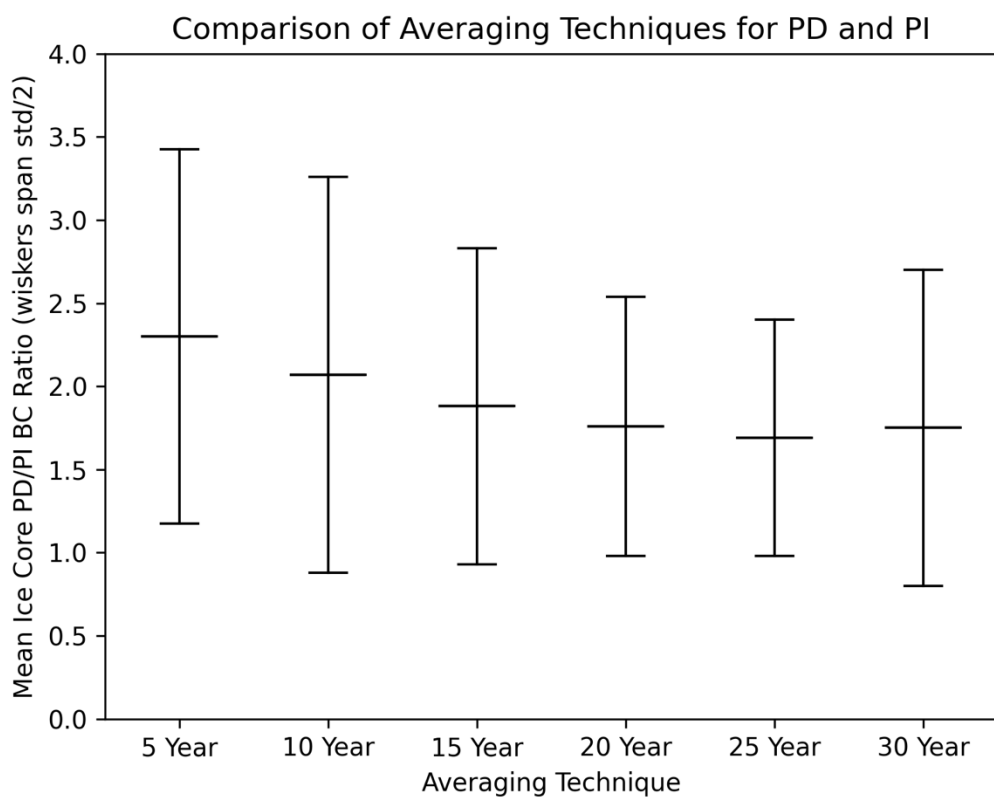


**Figure A4.** Comparison of averaging techniques for the ice cores' PD and PI.

Distribution of Mean Ice Core PD/PI BC Ratio Across Different Antarctic Regional Boundaries

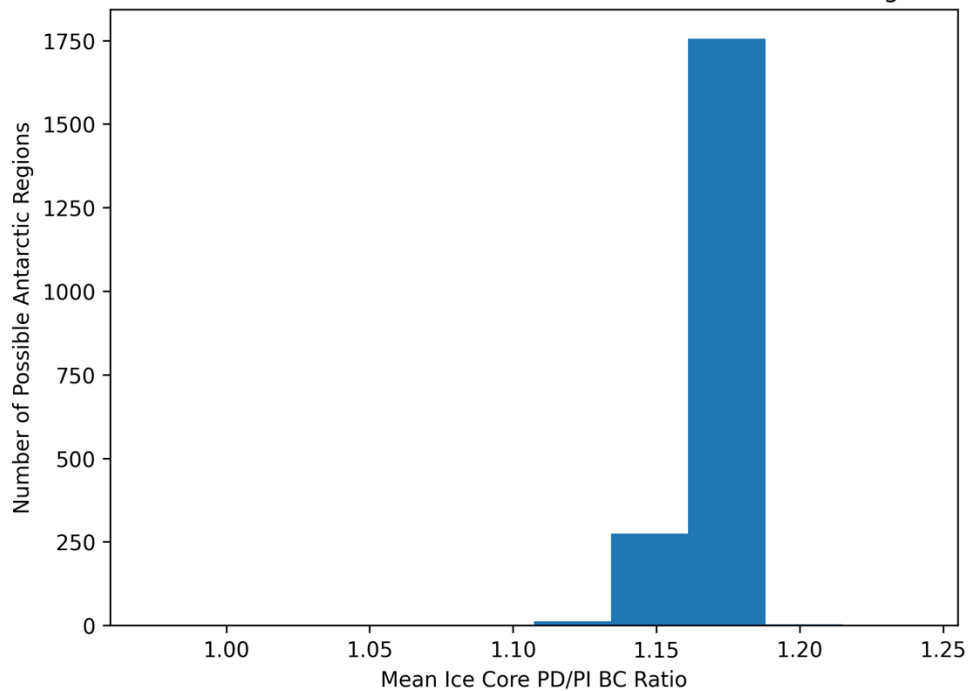


**Figure A5.** Histogram of every possible regional division of the Antarctic ice cores. All ice cores fall within a 0.1 PD/PI BC Ratio range.

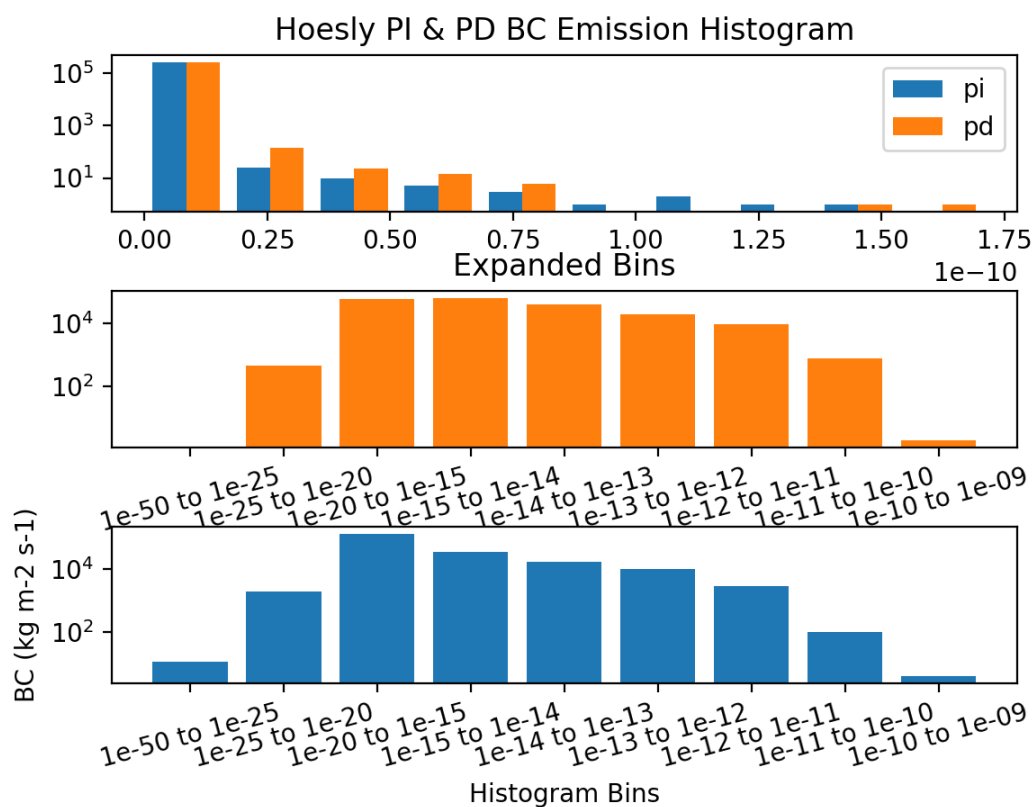


**Figure A6.** Histogram of global Hoesly anthropogenic BC emission sources in the PI and PD, highlighting low values less than  $10^{-25}$  in the PI that skew PD/PI ratios high.

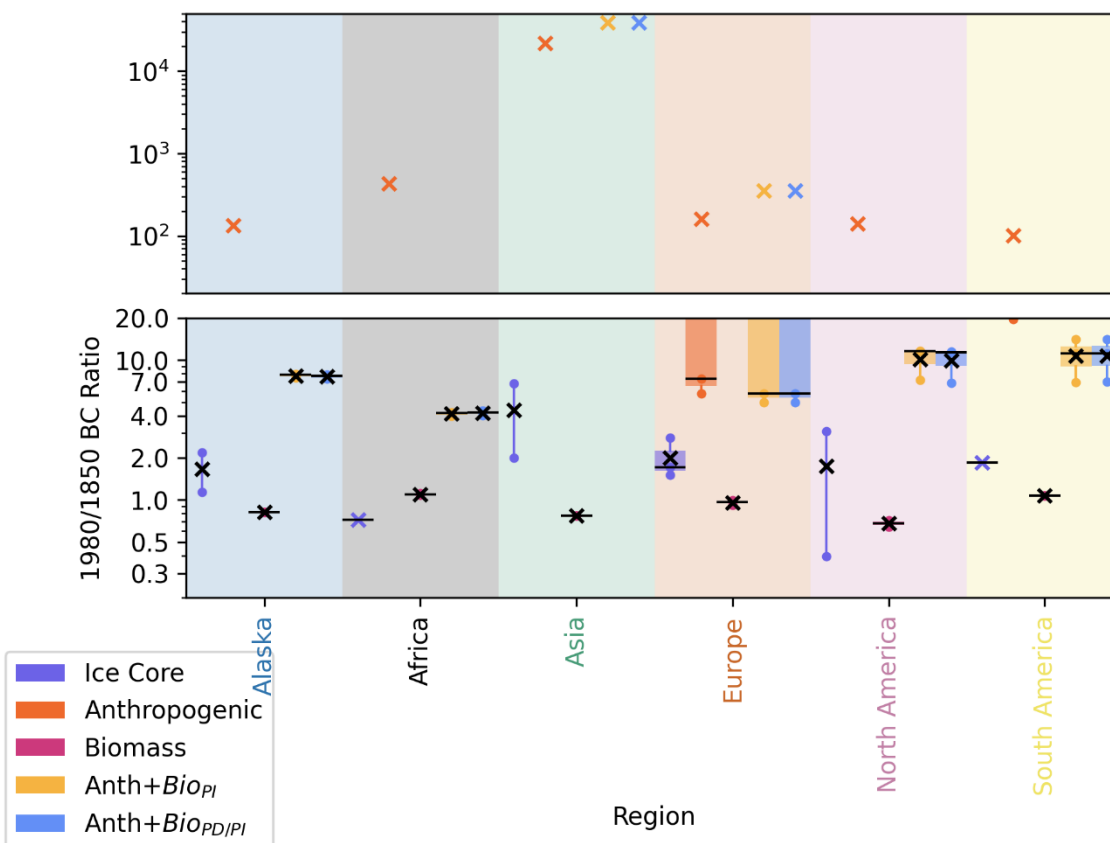


**Figure A7.** Using the emissions regions defined in section 2.3, results from Figure 3 were plotted against ice core values in Figure 4. These biomass PD/PI BC ratio means in each emission region (denoted with X's in Figure 3B) are relatively close to 1 (0.68 to 1.10), but are not within 40% of their corresponding ice core values in any region. Although 5/6 emission regions (Alaska, Asia, Europe, North America, and South America) showed mean Biomass ratios values below the ice cores', the Biomass BC dataset remains an overestimate because the combination Anthropogenic+Biomass PD/PI dataset, which best represents the total BC emissions that are captured by ice core records (as well as biomass, Anthropogenic+Biomass PI), all show regional ratio means above 400% of their corresponding ice core values, and frequently reach above 100, where the maximum ice core value in this dataset is 6.78.

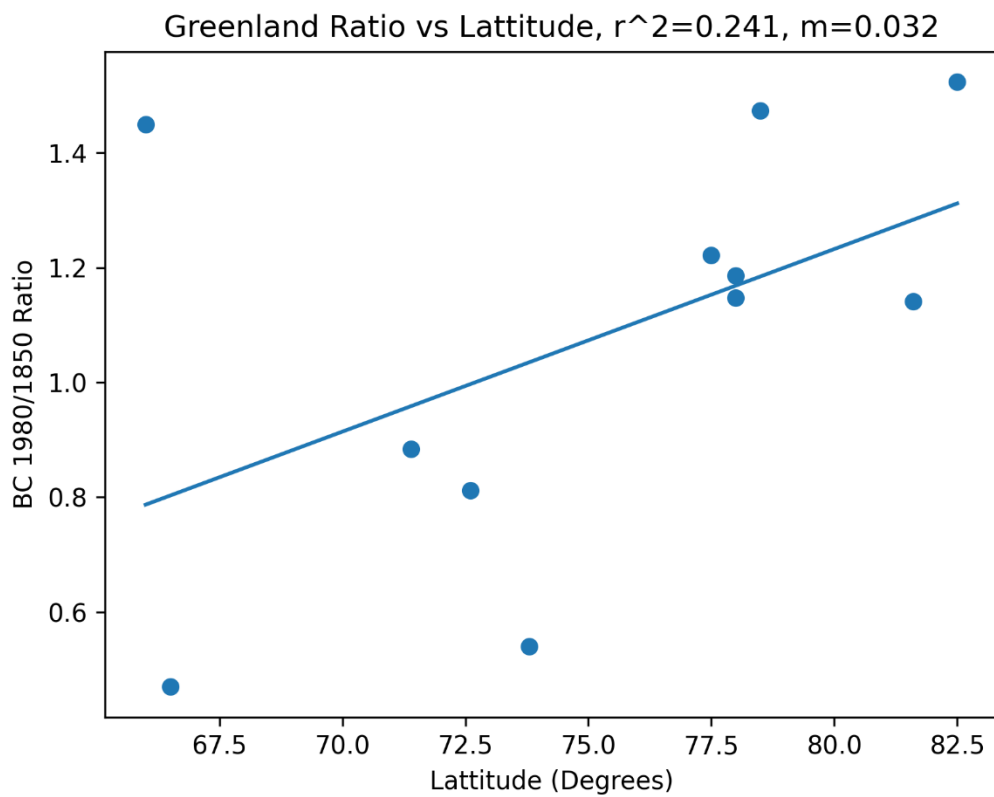


**Figure A8.** Correlation between Greenland ice cores' BC PD/PI ratio and latitude.

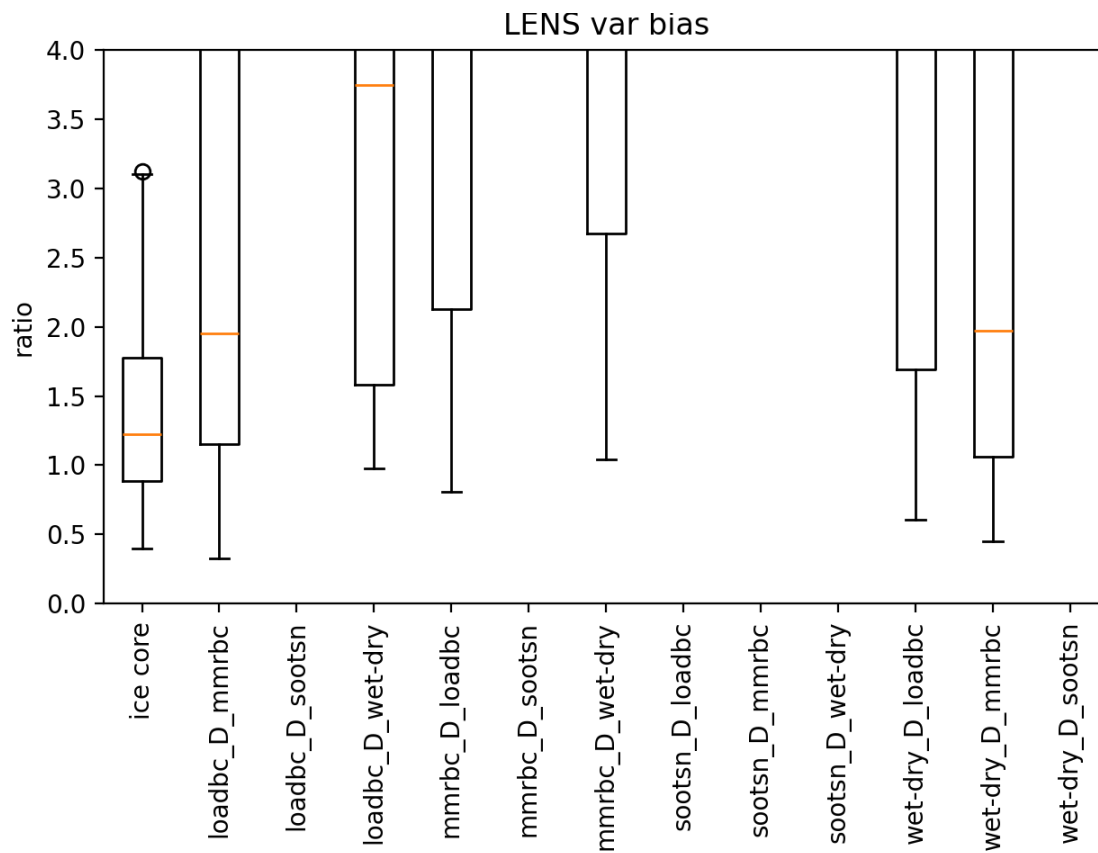


**Figure A9.** Comparison between various LENS variable biases (where  $\text{var1} \div \text{var2}$  is labeled as  $\text{var1\_D\_var2}$ ) and the ice core. Bias labels with no data shown have an first quartile bound above

4.

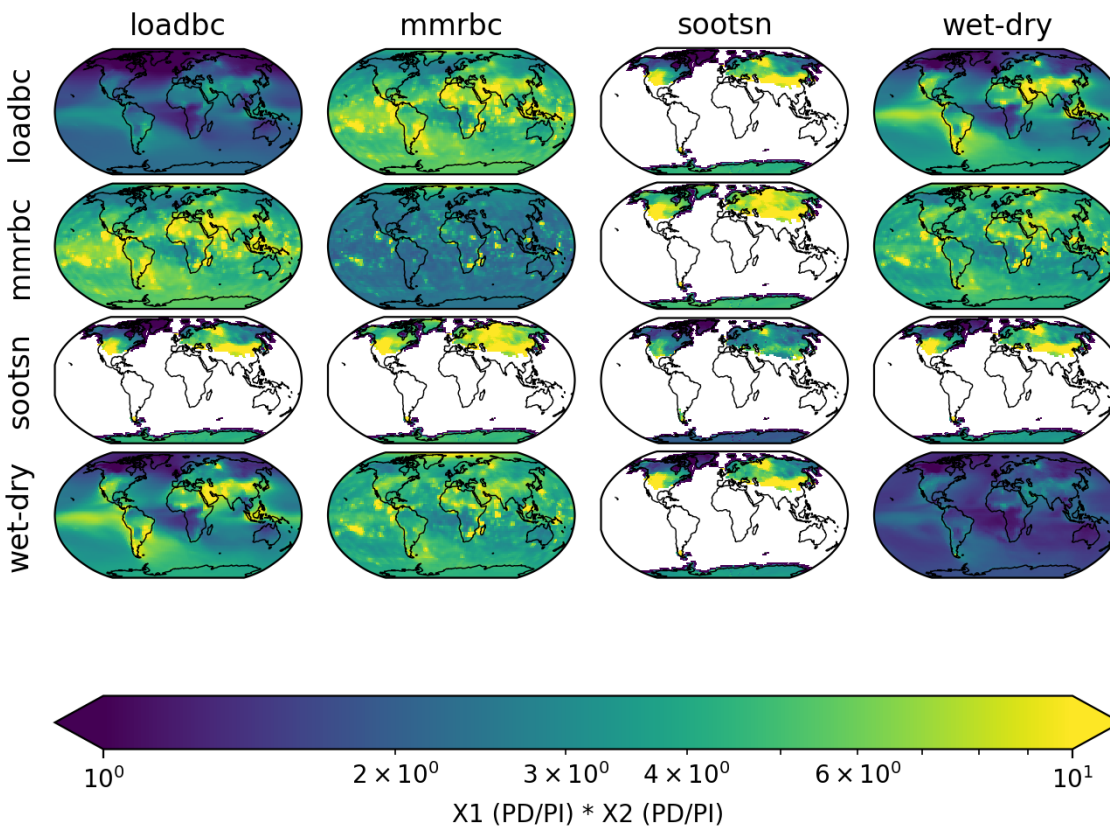


**Figure A10.** Relative PD/PI variable ratios. Each plot shows the PD/PI ratio of the variable in the column label multiplied by the ratio of the row label's variable. Plots on the diagonal show the raw PD/PI ratios from the single variable labeled. Missing data is also shown in white.

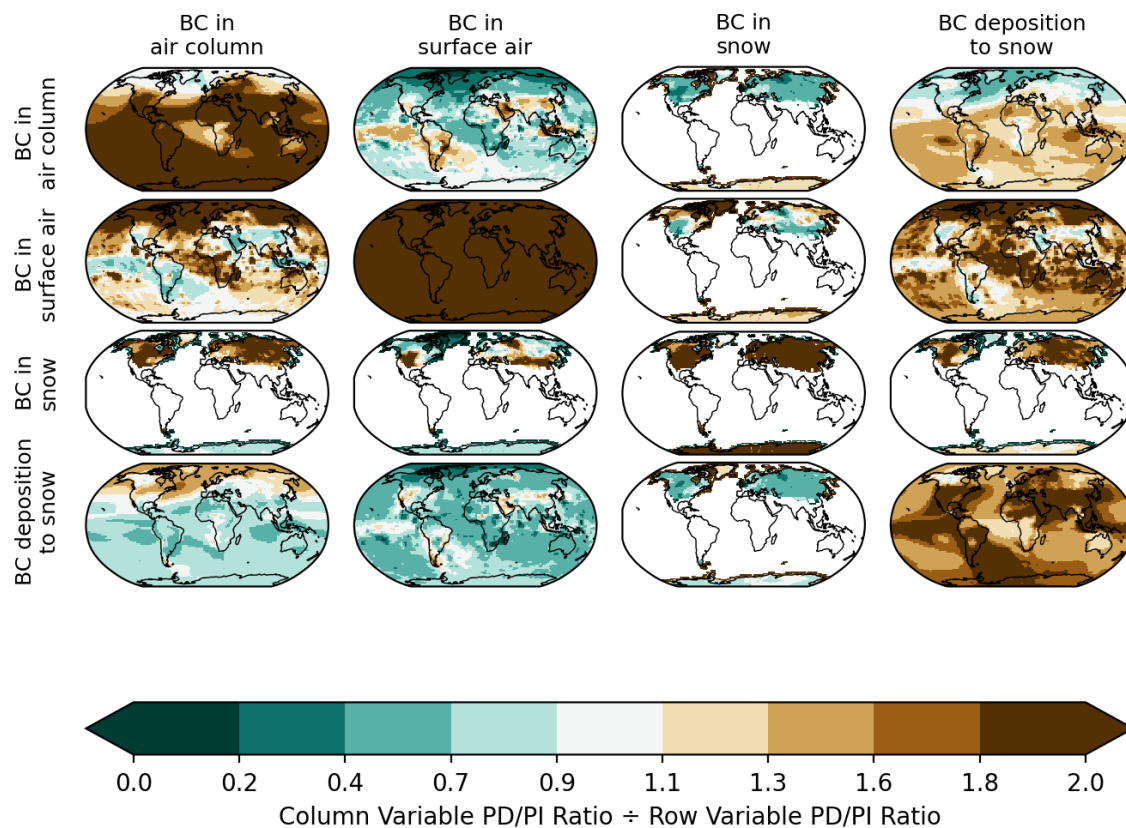


**Figure A11.** Relative PD/PI variable ratios. Each plot shows the PD/PI ratio of the variable in the column label divided by the ratio of the row label's variable. Plots on the diagonal show the raw PD/PI ratios from the single variable labeled. Ratios above 1, below 1, and near 1 are shown in brown, blue and white respectively. Missing data is also shown in white.

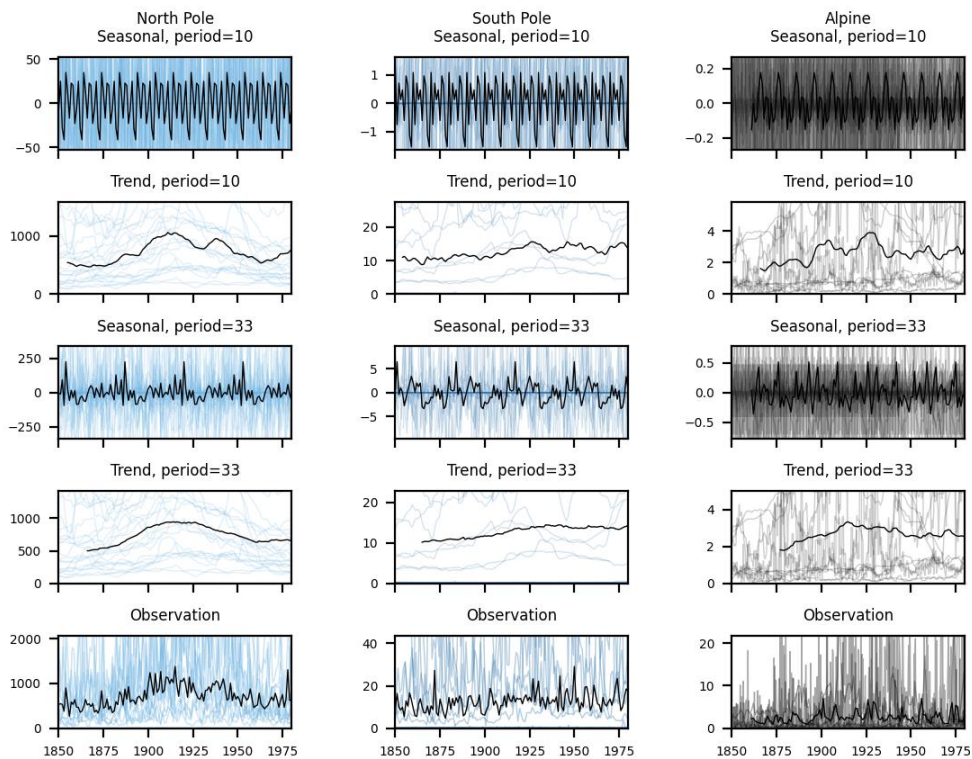


**Figure A12.** BC timeseries used in this work and their 10 and 33 year decompositions.

**Table A1.** Overview of the existing BC ice core model evaluation literature and this work's contribution to the literature.

	<b>Ours</b>	<b>Hamilton et al., 2018</b>	<b>Liu et al., 2021</b>	<b>Moseid et al., 2022</b>	<b>Zhang et al., 2024</b>
Number of Northern Hemisphere Ice Cores Used	24	4		15	16
Number of Southern Hemisphere Ice Cores Used	13		14	1	15
Compares individual model variables	X				

**Table A1.** (continued).

Compares different definitions of the pre-industrial and present day	X				
Model variables used	BC in air column, BC in surface air, BC deposition, BC in snow	BC in air	BC in air, BC deposition	BC deposition	BC deposition

**Table A2.** Comparison between different PI and PD averaging methods.

	<b>5 year PD and PI</b>	<b>10 year PD and PI</b>	<b>15 year PD and PI</b>	<b>20 year PD and PI</b>	<b>25 year PD and PI</b>	<b>30 year PD and PI</b>	<b>5 year PD and 25 year PI</b>
Mean ice core PD/PI BC ratio	2.30	2.07	1.88	1.76	1.69	1.75	2.10
Standard deviation in ice cores' PD/PI BC ratios	2.25	2.38	1.90	1.56	1.42	1.90	2.19
Minimum ice core PD/PI BC ratio	0.31	0.41	0.38	0.40	0.40	0.38	0.30
Maximum ice core PD/PI BC ratio	11.44	11.43	11.02	8.45	7.58	11.79	9.78

**Table A3.** Data sources, exact lat, lon positions, and abbreviations of each ice core.

Core Index	Publication Abbreviation	Data Source	Latitude	Longitude	Site/Abbreviation
1	Chellman et al. (2017)	<a href="https://doi.org/10.1021%2Facs.est.6b06574">https://doi.org/10.1021%2Facs.est.6b06574</a>	43.1	-109.6	Upper Fremont Glacier (WY)
2	Zhanget al. (2024)	<a href="https://doi.org/10.18739/A2KH0F13W">https://doi.org/10.18739/A2KH0F13W</a>	66.5	-46.3	ACT11d
3	Zdanowicz et al. (2018)	<a href="https://www.paldata.ca/pdcsearch/PDCSearchDOI.jsp?doi_id=12952">https://www.paldata.ca/pdcsearch/PDCSearchDOI.jsp?doi_id=12952</a>	75.32	-81.64	Devon ice cap
4	Zhanget al. (2024)	<a href="https://doi.org/10.18739/A2KH0F13W">https://doi.org/10.18739/A2KH0F13W</a>	73.8	-49.5	NasaU
5	Zhanget al. (2024)	<a href="https://doi.org/10.18739/A2KH0F13W">https://doi.org/10.18739/A2KH0F13W</a>	66	-45.2	ACT2
6	Zhanget al. (2024)	<a href="https://doi.org/10.18739/A2KH0F13W">https://doi.org/10.18739/A2KH0F13W</a>	72.6	-38.3	Summit2010
7	Zhanget al. (2024)	<a href="https://doi.org/10.18739/A2KH0F13W">https://doi.org/10.18739/A2KH0F13W</a>	69.3	-143.8	McCall_Glacier
8	McConnellet al. (2007)	<a href="https://doi.org/10.25921/bphv-jy23">https://doi.org/10.25921/bphv-jy23</a>	71.4	-44	D4

Table A3. (continued)

	Thompson et al. (2002)	<a href="https://doi.org/10.1126/science.1073198">https://doi.org/10.1126/science.1073198</a>	3.0766 67	37.3533 33	NIF2
9	Zhanget al. (2024)	<a href="https://doi.org/10.18739/A2KH0F13W">https://doi.org/10.18739/A2KH0F13W</a>	78.5	-56.8	Humboldt
10	Zhanget al. (2024)	<a href="https://doi.org/10.18739/A2KH0F13W">https://doi.org/10.18739/A2KH0F13W</a>	77.5	-51.1	NEEM_2011_S1
11	Zhanget al. (2024)	<a href="https://doi.org/10.18739/A2KH0F13W">https://doi.org/10.18739/A2KH0F13W</a>	78	-33.8	Tunu2013
12	Liuet al. (2021)	<a href="https://doi.org/10.6084/m9.figshare.14251022">https://doi.org/10.6084/m9.figshare.14251022</a>	66.769 444	111.580 833	W10
13	Zhanget al. (2024)	<a href="https://doi.org/10.18739/A2KH0F13W">https://doi.org/10.18739/A2KH0F13W</a>	82.5	-37.5	Hans_Tause n
14	Liuet al. (2021)	<a href="https://doi.org/10.6084/m9.figshare.14251022">https://doi.org/10.6084/m9.figshare.14251022</a>	-78.6	35.6	NORUS_7_5
15	Arienzo et al. (2017)	<a href="https://doi.org/10.15784/601034">https://doi.org/10.15784/601034</a>	-75	0.1	B40
16	Taylor et al. (2011)	<a href="https://doi.org/10.15784/600142">https://doi.org/10.15784/600142</a>	79.467 6	112.086 5	WAIS DIVIDE
17			-	-	

Table A3. (continued)

18	McConnellet al. (2022)	<a href="https://doi.org/10.18739/A2W37KX21">https://doi.org/10.18739/A2W37KX21</a>	81.6	-15.7	Flade Isblink
19	McConnellet al. (2021)	<a href="https://doi.org/10.15784/601464">https://doi.org/10.15784/601464</a>	-76.8	31.9	B53
20	Siglet al. (2018)	<a href="https://doi.org/10.1594/PANGAEA.894788">https://doi.org/10.1594/PANGAEA.894788</a>	45.932	7.876	CG15
21	Zhanget al. (2024)	<a href="https://doi.org/10.18739/A2KH0F13W">https://doi.org/10.18739/A2KH0F13W</a>	78	-36.4	NGT_B19
22	Liu et al. (2021)	<a href="https://doi.org/10.6084/m9.figshare.14251022">https://doi.org/10.6084/m9.figshare.14251022</a>	73.583 333	- 70.3666 67	Gomez
23	McConnellet al. (2021)	<a href="https://doi.org/10.15784/601464">https://doi.org/10.15784/601464</a>	-82.1	54.9	NORUS_7_ 7
24	McConnellet al. (2021)	<a href="https://doi.org/10.15784/601464">https://doi.org/10.15784/601464</a>	-74.1	1.6	NUS08_7
25	Ruppelet al. (2014)	<a href="https://doi.org/10.23728/fmi-b2share.858bbae80cde4b26bda0a37a56d7db99">https://doi.org/10.23728/fmi-b2share.858bbae80cde4b26bda0a37a56d7db99</a>	79.137 5	13.2722 22	Holtedahlfo nna glacier
26	Osmontet al. (2019)	<a href="https://doi.org/10.25921/3ygy-q259">https://doi.org/10.25921/3ygy-q259</a>	-16.65	- 67.7833	Illimani glacier

Table A3. (continued)

27	Legrandet al. (2023)	<a href="https://www.ncei.noaa.gov/access/paleo-search/study/38580">https://www.ncei.noaa.gov/access/paleo-search/study/38580</a>	43.348 3	42.4267	Mount Elbrus
28	Osmontet al. (2018)	<a href="https://doi.org/10.25921/gqct-0c60">https://doi.org/10.25921/gqct-0c60</a>	78.823 4	17.4331	LF-09
29	Zhanget al. (2024)	<a href="https://doi.org/10.18739/A2KH0F13W">https://doi.org/10.18739/A2KH0F13W</a>	60.5	-139.5	Eclipse
30	Matthewet al. (2016)	<a href="https://doi.org/10.1016/j.accre.2016.07.002">https://doi.org/10.1016/j.accre.2016.07.002</a>	33.576 667	91.1793 33	Guoqu glacier
31	McConnellet al. (2021)	<a href="https://doi.org/10.15784/601464">https://doi.org/10.15784/601464</a>	-64.2	-57.7	JRI_2008
32	Liuet al. (2021)	<a href="https://doi.org/10.6084/m9.figshare.14251022">https://doi.org/10.6084/m9.figshare.14251022</a>	- 71.166 667	111.366 667	Aurora_Bas in
33	Zhanget al. (2024)	<a href="https://doi.org/10.18739/A2KH0F13W">https://doi.org/10.18739/A2KH0F13W</a>	80.5	94.8	Akademii_ Nauk
34	Liuet al. (2021)	<a href="https://doi.org/10.6084/m9.figshare.14251022">https://doi.org/10.6084/m9.figshare.14251022</a>	-76.1	22.5	NORUS_7_ 2
35	Kaspariet al. (2020)	<a href="https://doi.org/10.1029/2019JD031126">https://doi.org/10.1029/2019JD031126</a>	48.356 389	- 121.057 4	SCG

**Table A3.** (continued)

36	Eichler et al. (2023)	<a href="https://www.ncei.noaa.gov/metadata/gpoportal/rest/metadata/item/noaa-icecore-37972/html">https://www.ncei.noaa.gov/metadata/gpoportal/rest/metadata/item/noaa-icecore-37972/html</a>	46.551	8.067	FH
37	Barker et al. (2021)	<a href="https://doi.org/10.25921/vxax-w749">https://doi.org/10.25921/vxax-w749</a>	28.383	3 85.7167	Dasuopu glacier

**Table A4.** Region definitions and number of ice cores.

<b>Large Region</b>	<b>Region</b>	<b>Definition</b>	<b>Number of Ice Cores</b>
North Pole	Arctic	All area above 66.6 degrees latitude except Greenland	5
	North Greenland	Greenland's land area above 71.5 degrees latitude	8
	South Greenland	Greenland's land area below 71.5 degrees latitude	3
South Pole	Antarctic	Continental Antarctica	11
Alpine	Africa	Continental Africa	1
	Asia	Continental Asia	2
	Europe	Continental Europe, Eastern Europe and the Middle East	3
	North America	All area in continental North America below 67 degrees latitude	3
	South America	Continental South America	1

**Table A5.** The ensemble, subset, and comparisons of each model used in this analysis.

<b>Ensemble</b>	<b>Ensemble Subset</b>	<b>Model</b>	<b>Deposition Comparison</b>	<b>3 Variable Comparison</b>
LENS		All LENS Runs	X	
CMIP6	CESM2	CESM2	X	X
		CanESM5	X	
		CESM2_re	X	
		MIROC	X	
		EC	X	
		MRI	X	
		CNRM	X	
		IPSL	X	

**Table A6.** The max, min, and mean absolute and standard deviation differences between different grid box averaging methods for LENS data. S4 and S8 represent averaging the 4 and 8 nearest grid boxes to an ice core's lat lon respectively, and S1 represents using the raw data from the nearest grid box without any grid box averaging.

	<b>Max</b>	<b>Min</b>	<b>Mean</b>
S4 - S1	2.43314331813518	-1.7782451329598281	-0.10204251825655358
S8 - S1	3.151898085541914	-2.6076508029747067	-0.1551673302441016
std(S4) - std(S1)	0.9733858921307288	-5.607736691603087	-0.5590165402367577
std(S8) - std(S1)	2.223883730919977	-7.754390111571624	-0.6746387035635895

**Table A7.** The absolute and standard deviation differences between different vertical level averaging methods for LENS data. LV30 and LV28 represent nearest and third nearest levels to the Earth's surface respectively.

	<b>Max</b>	<b>Min</b>	<b>Mean</b>
LV30 - LV28	8.60E-3	7.04E-8	2.59E-4
std(LV30) - std(LV28)	2.15E-3	5.33E-7	2.67E-4

**Table A8.** Regional PD/PI BC medians from model variables.

<b>Regions</b>	<b>Ice Core</b>	<b>BC in air column</b>	<b>BC deposition to snow</b>	<b>BC in surface air</b>	<b>BC in snow</b>
North Pole	1.166662856	3.015009692	3.861902496	2.63879567	1.975689775
South Pole	1.050102303	3.1402834	3.255306975	2.58785237	1.909287804
Alpine	1.92523059	3.692888878	2.750148522	2.670535394	3.895460773

**Table A9.** Regional PD/PI BC means.

<b>Region</b>	<b>Ice Core</b>	<b>Hoesly</b>	<b>Marle</b>	<b>Hoesly+MarlePI</b>	<b>Hoesly+MarlePD/PI</b>
Alaska	1.67	133.73	0.82	7.74	7.63
Africa	0.72	431.5	1.1	4.13	4.2
Asia	4.4	21704.17	0.77	39013.48	39013.4
Europe	2	158.96	0.96	356.42	356.41
North America	1.75	139.45	0.68	10.14	9.9
South America	1.84	100.78	1.07	10.68	10.72
Global Mean	2.06	3778.1	0.9	6567.1	6567.04